MEASUREMENT AND OPTIMIZATION OF THERMAL TRANSPORT PHENOMENA FOR WELD STRENGTH IMPROVEMENT IN POLYMER EXTRUSION BASED ADDITIVE MANUFACTURING

by

DARSHAN RAVOORI

Presented to the Committee Members

Dr. Ankur Jain (Committee Chair)

Dr. Ashfaq Adnan

Dr. Amir Ameri

Dr. Narges Shayesteh

Dr. Emma Yiran Yang

of The University of Texas at Arlington in Partial Fulfillment

of the Requirements

for the Completion of

DOCTOR OF PHILOSOPHY

THE UNIVERSITY OF TEXAS AT ARLINGTON

May 1st, 2020

I dedicate this thesis to

my father and pummy

ACKNOWLEDGEMENT

Firstly, I would like to thank my advisor Prof. Ankur Jain for the continuous support of my Ph.D. In my mind, I always want to do research on heat transfer related to process improvements of given system. When I first met Prof. Ankur Jain, I asked good number of questions related to his research on heat transfer and how he approaches the problem and provide a solution. Later, I expressed my interest to work on thermal transport phenomena in the polymer additive manufacturing and Prof. Ankur Jain opened the doors for me into Microscale Thermophysics Lab, where first steps of my Ph.D journey began. I am very grateful for his patience, motivation, and immense knowledge shared with me. He is very supportive and given me the freedom to explore various projects without objection.

I am thankful to professors Ashfaq Adnan, Amir Ameri, Narges Shayesteh, Emma Yiran Yang for their time to review my work as a part of dissertation committee members and shared their valuable feedback about my research work. My sincere thanks to Hardikkumar Prajapati, Swapnil Salvi, Mohammad Parhizi, Amirhossein Mostafavi, Dhananjay Mishra and to my collaborators Viswajit Talluru, Momen Qasaimeh and past members of MTL Aditya Krishna, Krishna Shah, Vivek Vishwakarma and Swapnil Luhar. They provided immense support whenever I ran into a problem or having questions related to equipment operation or any concept.

In the end, I am grateful to my parents, sister, wife and pummy who always hoped

for my ultimate success. Without their support and encouragement to achieve my goals, I would not be what I am today. My wife has always supported me financially so that I can dedicate my entire time on research without facing any financial hardship during my Ph.D journey.

ABSTRACT

THERMAL TRANSPORT PHENOMENA IN POLYMER ADDITIVE MANUFACTURING

Darshan Ravoori

The University of Texas at Arlington, 2020

Supervising Professor: Ankur Jain

Additive manufacturing (AM) processes involve layer-by-layer addition of material to fabricate a 3-dimensional part. AM offers significant design and manufacturing flexibility compared to traditional manufacturing approaches. The major challenge in polymer-based additive manufacturing (AM) is that printed parts often have poor thermal/structural properties. These properties depend on weld strength of filaments and which intern depends on the degree of healing/neck growth between deposited polymers. The major contribution of this dissertation is understanding the importance of heat transfer during the printing process on the polymer neck growth and presented with techniques to improve the thermal and structural strength of finished part.

At first dependence of thermal conductivity of polymer AM parts on the print process parameters is studied. This research developed the understanding through a combination of in-situ high speed imaging and thermal conductivity measurements. Subsequently, measurement of temperature distribution of

deposited layer onto pre-deposited layers through in situ infrared thermography is carried out. Degree of healing (weld formation/neck growth) between two polymer filaments deposited is directly governed by heat transfer. This dissertation work measured the temperature profile of the single filament deposited through infrared thermography and showed that hot nozzle tip causes significant temperature to rise in the pre-deposited layer before filament deposition.

A novel concept of in situ, nozzle-integrated pre- and post-heating of previously deposited filaments is implemented, and improved weld formation compared to the baseline case is demonstrated. This research work addresses the key broader challenge in polymer AM by developing a novel approach for thermal enhancement of filament-to-filament neck growth process. This is expected to result in parts with improved properties that can be used in applications involving thermal and mechanical loads. Optimization of pre-post heater temperature is carried out to achieve required degree of healing between the filaments. It is expected that with pre-post heating of pre-deposited layers, weld strength improves resulting in higher mechanical strength which intern reduces the void percentage.

The experimental study present in this dissertation enables optimization of thermal conductivity of polymer AM parts by developing relationships between print process parameters and thermal properties of interest in a variety of applications. Estimation of heat transfer from newly deposited layer into pre-

deposited layers is studied through in-situ IR measurements and demonstrated that classical welding moving heat source analytical solution can be used to predict the temperature profiles of weld zone between two filaments. Further demonstration of novel pre-post heating of polymer layers overcomes the drawback of poor structural strength (due to voids) in polymer AM.

LIST OF FIGURES

LIST OF TABLES

TABLE OF CONTENTS

CHAPTER 1

INTRODUCTION

Additive Manufacturing (AM) [1-3] offers several advantages compared to traditional manufacturing methods, and therefore, is currently being investigated for a wide variety of applications [4-7]. Broadly, AM techniques can be classified into two categories – metal-based AM involving processes such as Selective Laser Sintering (SLS) [8-9], or polymer extrusion based AM [10-11]. These techniques offer increased design flexibility, capability of producing nearly-arbitrary shapes and the possibility of tailored properties of printed parts [1-2]. In polymer extrusion processes, a polymer filament is heated to above the glass transition temperature and extruded on to a platform [10]. The extruded polymer lines – often referred to as roads – merge into neighboring lines as they cool, thereby imparting mechanical strength and rigidity to the built part. Multiple layers of such polymer lines are dispensed on top of previously built layers, and the shape of the part is controlled by spatially selective deposition of polymer filament in each layer. A large amount of literature exists on understanding and optimizing the polymer extrusion based AM process [10,12-14], including the various sub-processes such as filament heating, extrusion, deposition, as well as post-process treatment.

The merging of adjacent polymer roads into each other plays a key role in determining the microstructure, and hence the overall properties and performance of the built part [10]. This is a dynamic process that is likely to depend on a number of process parameters, such as raster speed, extrusion temperature, etc., as well as

the properties of the polymer material such as glass transition temperature, temperature-dependent viscosity, surface tension, etc., some of which have been investigated in the past [12-14]. Multiple highly coupled physical processes occur during the merging process, including cooling and glass transition, surface tension driven flow and integration of polymer strands between adjacent roads [12]. Understanding and optimizing these processes and their interactions is critical for obtaining desired microstructure, and ultimately for obtaining properties of interest in the built part. Several papers have carried out theoretical and numerical modeling of the filament extrusion and deposition process, including theoretical models [15-16] and numerical simulations [17-18] to predict thermal profiles following deposition. While these studies provide much needed theoretical insight into the microscale processes underlying polymer extrusion AM, there is also a need for correlating these processes with the properties of the built part, for example, by connecting these properties with the microstructure resulting from various process parameters. *In situ* visualization of the AM process, particularly the dispensing and merging of adjacent roads, and post-process property measurement could play a key role in developing these correlations.

A number of studies have investigated the effect of various process parameters on the ultimate properties of the built part [19-23]. Most of these studies have focused on mechanical and structural properties such as mechanical strength, Young's modulus, etc. Anisotropic mechanical properties have been reported as a function of print speed and raster orientation [22]. Tensile strength has been shown

to correlate with layer height [24]. Raster angle of 0º and 90º has been shown to result in maximum and minimum tensile strength respectively. The latter is shown to fail in transverse load because the load is taken up by the bonding between fibers and not the fibers themselves [19]. Tensile strength of criss-cross rastering has been shown to fall in between the two extremes [19]. In comparison to the considerable literature on mechanical properties, there is relatively lesser work available on thermal properties of built parts and their relationship with microstructure and process parameters. These properties, such as thermal conductivity govern the nature of heat flow through the part [25], and therefore, are critical for understanding the performance of the part in an engineering application where heat generation and heat flow may be important considerations. Similar to mechanical properties such as mechanical strength, it is reasonable to expect that thermal conductivity will be influenced by the microstructure of the built part. For example, the extent of adhesion between adjacent roads may influence the amount of heat flow, and hence the value of the thermal conductivity. Specifically, poor adhesion resulting from incorrectly designed process parameters is expected to lead to insufficient heat flow, and hence poor thermal conductivity.

Clearly, there is a need to identify optimum process parameters that result in parts with desired thermal properties. The relationships between process, microstructure and properties have not been sufficiently studied in the context of thermal performance of built parts. The effect of sintering on filament bonding has been studied [16]. However, this is a post-printing process, whereas it would be

more effective to understand and optimize parameters related to the printing process itself, in order to result in desired thermal properties.

Further, several applications call for multifunctional parts that must perform both thermal and structural function. For example, structural parts often need to provide thermal insulation as well. In such a case, it is critical to optimize the process parameters and microstructure in order to obtain a balance between mechanical strength and thermal conductivity, along with weight considerations. Addressing this complicated problem requires an integrated approach involving both microscale visualization to understand microstructure, as well as part-scale measurement of thermal properties to fully understand the impact of process parameters on thermal properties. Such an approach, while entailing multiple experimental challenges is expected to enhance the fundamental understanding of polymer extrusion based AM, as well as result in optimized build strategies for specific parts.

Chapter 2 presents results from high speed, microscale visualization of polymer extrusion based additive manufacturing integrated with thermal property measurements. High speed imaging of the process is carried out for different values of the key process parameters such as raster speed, layer height, etc. These images are used to determine the dependence of microstructure on process parameters. The variation of thermal properties of the built part on process parameters is characterized through measurement of thermal conductivity in the build direction

based on a one-dimensional heat flux method. Results indicate strong dependence of thermal conductivity on raster speed and layer thickness, which is corroborated by high speed imaging of the printing process at different values of these process parameters. The extent of inter-layer adhesion expected from imaging experiments correlates well with thermal conductivity measurements of built parts. These results are expected to extend the fundamental understanding of microscale processes underlying polymer based AM and their relationships with the properties of the eventual part, particularly in the context of thermal properties. Process optimization carried out based on these results may be instrumental in designing and building parts with desired, multi-functional properties.

The process of merging of discrete polymer lines into each other to form the final part is at the core of the polymer AM process [1,32]. The nature and extent of such merging ultimately determines the properties of the final part such as Young's modulus, thermal conductivity, etc. [19,24,32]. Therefore, it is critical to understand how process parameters influence the filament bonding process. Clearly, heat transfer plays a critical role in this process. Heat transfer occurs from one filament to the other, from filaments into the bed and from filaments into the ambient [33,34]. These heat transfer processes determine the temperature history of the merging filaments. It is of interest, for example, to optimize the underlying heat transfer processes and enable the filaments to stay at a temperature greater than the glass transition temperature for a long time in order to facilitate effective merging of the filaments.

A few papers have carried out experimental measurements of heat transfer processes during the merging of polymer filaments on a bed. Note that the bed on which the filaments are deposited may comprise either previously deposited layers or, in the case of the first layer, the build plate on which the part is printed. Infrared thermography, a non-invasive temperature measurement technique, with extensive past work related to microelectronics and microelectromechanical systems (MEMS) [35-37] offers the capability of measuring the entire temperature field with good spatial and temporal resolution. Infrared thermography has been used for measuring temperature distribution on the bed as a function of depth [38], although these data have not been compared with theoretical models. Filament temperature distribution in the standoff region has also been measured using an infrared camera [39]. Process monitoring for fabricating thin wall composites has been reported using infrared thermometry [33], showing that temperature plays a key role in the degree of warping and cracking in the thin walls. Embedded micro-thermocouples have also been used for temperature measurement, although this approach only provides a local temperature measurement [16]. Post-process annealing has been investigated as a possible mechanism for improving filament-to-filament bonding, and therefore the overall strength of the final part [15]. Heat transfer processes prior to filament deposition, including polymer melting and extrusion through the nozzle, as well as heat transfer in the standoff region between nozzle tip and bed have also been measured [39,40,41].

Theoretical and numerical analysis of heat transfer processes in polymer AM has also been presented in several papers. Analytical models based on principle of energy conservation in the deposited filament have been presented, although this model accounts for filament-to-bed heat transfer only through a convective heat transfer coefficient [15]. Heat transfer between filaments and between filament and bed has been analyzed based on areas of contact, resulting in prediction of the quality of bonding [34]. Both lumped [16,15] and two-dimensional finite element [33] models are available. Finite-element analysis has been carried out for predicting temperature distribution on the platform bed [42]. From a heat transfer perspective, the rastering of the filament on the platform bed can be described as a moving heat source [43]. This approach has been used extensively for thermal modeling of processes such as welding [44,45,46], but no application of moving heat source theory for polymer AM appears to exist.

Clearly, there is a need for systematic measurements and modeling for quantifying the heat transfer processes that influence the temperature distribution in the layer being printed and in previously printed layers underneath, as this critically affects the extent and quality of bonding between adjacent filaments. Since the hot filament dispensed on the bed has greater energy due to its high temperature relative to the bed, it will clearly result in bed temperature rise once deposited. In addition, due to the short standoff gap between nozzle tip and bed, and the relatively high nozzle tip temperature, heat transfer from nozzle tip to bed in the form of thermal conduction and/or radiation may also be an important process

in the dynamics of bed temperature as the nozzle tip rasters over the bed. A careful theoretical analysis of these phenomena, when combined with experimental measurement of the temperature field may help understand the fundamentals of heat transfer in polymer AM, and hence lead to design tools for engineering the thermal and mechanical properties of the built part.

Chapter 3 presents experimental measurement of temperature distribution on the bed using infrared thermography and comparison with a theoretical model based on moving heat source theory in a broad range of process parameters. Experiments without and with filament dispense from the hot nozzle tip identify and quantify the contributions of thermal energy deposited with the filament and heat transfer from the hot nozzle tip on the bed temperature, showing that the nozzle tip plays a significant role in this process. Experimental data at a number of raster speeds and nozzle-to-bed gaps are found to be in good agreement with theoretical heat transfer models. Measurements of temperature decay in a filament after completion of the dispense process are also presented. These measurements and models offer previously unavailable insight into the process parameters that affect temperature distribution on the platform bed during polymer AM, which can be used for engineering the quality of bonding between adjacent filaments in polymer AM.

Section 3.2 describes the experimental setup for infrared thermography measurements. Theoretical model for temperature distribution on the bed due to a

moving heat source is described in Section 3.3. Key results are presented and discussed in Section 3.4.

Given the increased recent interest in additively manufactured multifunctional parts, the thermal and mechanical properties of additively manufactured parts, and the impact of process parameters on these properties has been studied extensively [16,19,24,27,32,42]. The polymer AM process involves the dispensing of a filament that is heated in a nozzle to a temperature greater than the glass transition temperature or melting temperature, for amorphous and semi-crystalline polymers, respectively, e prior to dispensing the material. Following deposition, adjacent filaments merge into each other while cooling down. As the temperature approaches the glass transition temperature, the polymer becomes extremely viscous, thereby stopping neck growth between filaments [34,49]. The thermally-driven neck growth and merging between filaments is the fundamental process that imparts mechanical strength and good thermal conductivity to the part [19,27,32]. Experiments have shown that maintaining previously deposited layers at a high temperature results in improved inter-layer bonding [50,51]. As a result, heat transfer during the filament deposition process plays a key role in determining overall properties of the part.

Research on experimental and theoretical/numerical investigation of heat transfer during polymer AM has been presented in the past. Heat transfer modeling of the AM process has been carried out with varying degrees of detail, including

one-dimensional [15] and three-dimensional analytical modeling [52], finite-element simulations [33,42], etc. Infrared thermometry based measurements of temperature distribution in the stand-off gap [19] and around a deposited filament have been presented [52,53]. Temperature distribution around the deposited filament has been shown to be influenced by the thermal energy of the deposited filament, as well as heat transfer directly from the hot nozzle [52]. Through both experiments [32,52] and modeling [34,42], process parameters such as raster speed, filament diameter, etc. have been shown to play a key role in determining the rate of cooling of the filament. Both measurements and theoretical models show very rapid temperature drop in and around the filament, underscoring the critical need for optimizing heat transfer during polymer AM to ensure that the filament stays above glass transition temperature for as long as possible.

The important role played by temperature and heat transfer in determining the properties of the printed part is also highlighted by papers that investigate post-process thermal annealing [54,55,56]. A variety of experiments have reported significant enhancement in thermal and mechanical properties of polymer printed parts exposed to a high temperature for a certain time after printing. Both annealing time and temperature have been shown to influence the enhancement [54,55], which appears to occur due to improved filament-to-filament bonding when subjected to high temperature for a period of time.

Both sets of past work described above suggest the importance of maintaining a high temperature in and around the filament for as long as possible. Some possible process-related changes to enable this include increasing the nozzle temperature, reducing the thermal diffusivity of the filament material, maintaining the build chamber at a high temperature, etc. Clearly, there are practical limitations for these approaches, since, for example, thermal conductivity of the filament is fixed by the material choice, and the nozzle temperature can not be made too high because of undesirable changes in material properties at high temperature. Changing the raster speed is also unlikely to be effective, as this has been shown to not influence the peak temperature or rate of temperature reduction, and may actually inhibit neck growth between filaments [32].

A few approaches for external heating of the deposited filaments have been investigated in the past. For example, a near-IR laser beam has been focused using an elaborate set of mirrors and other optics to provide local pre-heating prior to filament deposition [57]. An infrared lamp has also been used for preheating [58]. Microwave heating has been utilized for raising the local temperature during polymer AM [59]. These papers report increased local temperature and enhanced filament-to-filament adhesion due to localized heating. However, each of these approaches requires additional, expensive equipment and result in complications in the process flow. A passive approach for preheating of previously deposited layers is highly desirable.

One possible approach for increasing the time duration for which the deposited filament remains at high temperature is to provide an extended, hot surface that rasters along with the nozzle as shown schematically in Figure 1(a). Past work has already shown that heat transfer from the hot nozzle surface influences temperature distribution on the previous deposited layers [52]. Consequently, the presence of a hot metal block that moves along with the nozzle may further increase temperature of previously deposited layers and keep the present layer at an elevated temperature for a longer time. Compared to other approaches investigated in the past, such as laser [57], infrared [58] and microwave [59] heating, this approach significantly reduces the physical distance between the heater and print bed (1-2 mm in the present work compared to around 8 cm in infrared heating [58]). As a result of the much lower gap, the heater provides adequate heating without needing to be maintained at a very high temperature such as an IR heater. Due to the tight integration with the nozzle, the present approach is relatively passive and easy to implement, since a heating mechanism, usually through Joule heating, is already being used to heat up the nozzle barrel and can be easily extended for the hot metal block without much added cost or complexity.

Chapter 4 presents experimental and theoretical analysis of the heating of previously deposited layers using a hot metal surface that rasters close to the base along with the dispensing nozzle. Two configurations are analyzed – a preheater configuration in which the hot metal surface rasters ahead of the nozzle, and a postheater configuration in which the hot metal surface rasters behind the nozzle.

Temperature measurement based on infrared imaging is carried out. As expected, the preheater and postheater configurations result in significant temperature increase before and after filament dispense respectively. A configuration with both preheater and postheater is also analyzed. The extent of temperature increase is found to be a strong function of the gap between heater and bed surface, as well as the raster speed. Experimental data are found to be in good agreement with a mesh deformation based finite-volume simulation model. Cross-section imaging of printed parts clearly shows significant impact of this approach on filament-to-filament neck growth.

Section 4.2 describes the experimental setup for integrating preheater and postheater configurations into the polymer AM process as well as infrared thermography measurements. Theoretical and finite-volume simulation modeling is discussed in section 4.3. Key results are presented and discussed in Section 4.4.

CHAPTER 2

INVESTIGATION OF PROCESS-STRUCTURE-PROPERTY RELATIONSHIPS IN POLYMER EXTRUSION BASED ADDITIVE MANUFACTURING THROUGH IN SITU HIGH SPEED IMAGING AND THERMAL CONDUCTIVITY MEASUREMENTS

Ravoori, D., Alba, L., Prajapati, H., Jain, A., 'Investigation of process-structure-property relationships in polymer extrusion based additive manufacturing through in situ high speed imaging and thermal conductivity measurements,' *Additive Manufacturing*, 23, pp. 132-139, 2018.

2.1. Experiments

Experiments are carried out to identify the dependence of build direction thermal conductivity, k_z on various process parameters including extruder print speed, layer height and infill percentage. *In situ* visualization of the rastering process is carried out using high speed imaging, which helps identify the key microstructural features of the built part and correlates these with process parameters. In addition, thermal conductivity measurements are carried out on the built parts in order to understand the effect of process parameters and microstructure on the resulting thermal properties of the part.

2.1.1. Fabrication of test samples

Fabrication of samples is carried out on a polymer extrusion based, open source 3D printer using 1.75 mm diameter black polylactic acid (PLA) material. The process parameters studied in this work include raster speed, infill percentage and layer height. Raster speed is varied in the 1000–18000 mm/min range, while infill percentage is varied between 50% and 95%. Layer height in the 0.2-2.5 mm range is investigated. Print temperature is held constant at 215 ºC, and a 0.4mm diameter nozzle is used in all experiments. Two samples of thicknesses 4 mm and 8 mm are printed for thermal conductivity measurement as outlined in section 2.3. Each sample has a size of 40 mm by 40 mm. Geometry for each sample is modeled in Solidworks and exported to Simplify3D software for slicing. The G-code generated in this manner is directed to the 3D printer for printing with specified build process parameters.

2.1.2. *In situ* high speed imaging

In situ high speed imaging of the polymer printing process is carried out in order to understand the process of adhesion between adjacent lines, and correlate the microstructure of printed lines with process parameters on one hand, and thermal properties of the printed part on the other. A FASTEC Imaging IL5SM4 high speed camera is arranged at a sideways angle in order to view the rastering process. In conjunction, a Navitar 12V 150W high intensity fiber optic illuminator source is used for improving the image quality. Videos of the rastering process are recorded at a rate of 120 frames per second, with minimum 3μs shutter time and pixel size of 5μm by 5μm. Figure 2.1 (a) shows a picture of the experimental setup, showing the 3D printer, as well as the high speed camera and illumination used for video capture.

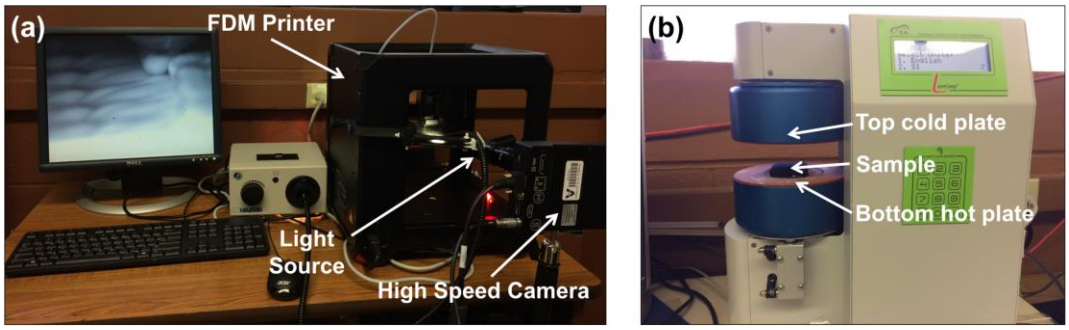

Figure 2.1. (a) Picture of experimental setup showing the 3D printer, high speed camera and high intensity light source; (b) Picture of thermal conductivity measurement setup.

The *in-situ* high speed imaging during the rastering process is supplemented with post-processing cross-section imaging of printed samples. In order to preserve the internal microstructure of parts during the cutting process, samples are cut

carefully using liquid nitrogen. Four small notches are first made on the four edges of the sample of interest. The sample is then immersed in liquid nitrogen for two minutes, and an impact load in applied on one of the notches. Cross sections of cut samples are imaged using a 10 megapixel AMScope microscope digital camera in conjunction with an AmScope 3X stereomicroscope.

2.1.3. Thermal conductivity measurements

Thermal conductivity of the built parts is measured in the build direction by applying a temperature difference across a test sample and measuring the resulting heat flux using the Fox50 thermal conductivity measurement instrument. Figure 2.1(b) shows a picture of the experimental setup for thermal conductivity measurement. A picture of the representative samples of two different thicknesses (4mm and 8 mm) is shown in Figure 2.2.

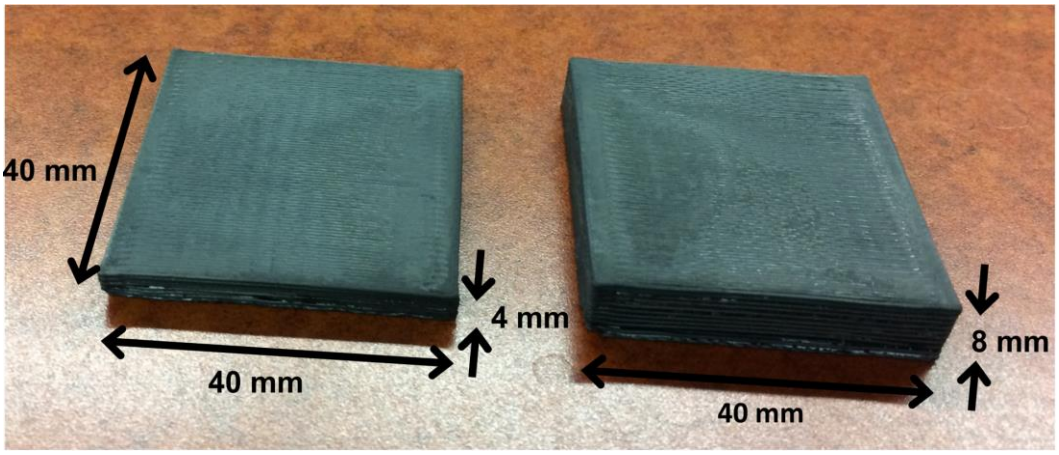

Figure 2.2. Pictures of 4 mm and 8 mm thickness samples with 40 mm by 40 mm sides printed for thermal conductivity measurements.

In order to account for interfacial thermal contact resistance between the

sample and the instrument during thermal conductivity measurements, separate measurements are carried out on samples of two different thicknesses, and the difference between the total thermal resistances between the two samples is used to determine the thermal conductivity of the material.

The measured total thermal resistance, which is the ratio of temperature difference and heat flux, comprises contributions from thermal resistance from the sample material and from the two interfaces between the sample and instrument plates.

$$R_T = 2R_c + R_m \tag{1}$$

The material thermal resistance R_m in equation (1) is given by L/k, where L and k are the thickness and thermal conductivity of the sample respectively. Assuming that interfacial thermal resistance, R_c, is the same for two samples of thicknesses L_1 and L_2, the thermal conductivity of the sample material may be determined from the measured total thermal resistance R_{T1} and R_{T2} for the two samples by eliminating R_c as follows [26]

$$k = \frac{L_1 - L_2}{R_{T1} - R_{T2}} \tag{2}$$

A guard wall is used around the sample during measurements for minimizing lateral heat loss. The instrument is calibrated by measuring thermal conductivity of standard pyrex samples of two different thicknesses using this

method, which results in very close agreement with the standard value (1.11 W/mK vs. 1.09 W/mK). Measurements are carried out on multiple sets of samples printed with different process parameters. Variation of thermal conductivity with infill percentage, layer height and raster speed is analyzed and correlated with imaging of the rastering process through the high speed camera.

2.2. Results and discussion

2.2.1. Progression of the polymer rastering process

Figures 2.3(a) through 3(d) show images of the rastering process captured at 1 s intervals during the printing process at 6000 mm/min speed, 100% infill and 0.4 mm layer height. In reference to these images, the polymer lines are printed from bottom to top of the image, and the extruder moves towards the left after printing each line. The structure of deposited lines is clearly seen in these images, which appear to adhere well with their neighboring lines. The underlying layer of lines deposited orthogonally prior to the present layer, as well as the nozzle head are also visible in these images. Figures 2.3(a) through 2.3(d) represent successive images of the process captured for a baseline case. The effect of changing various parameters is investigated next.

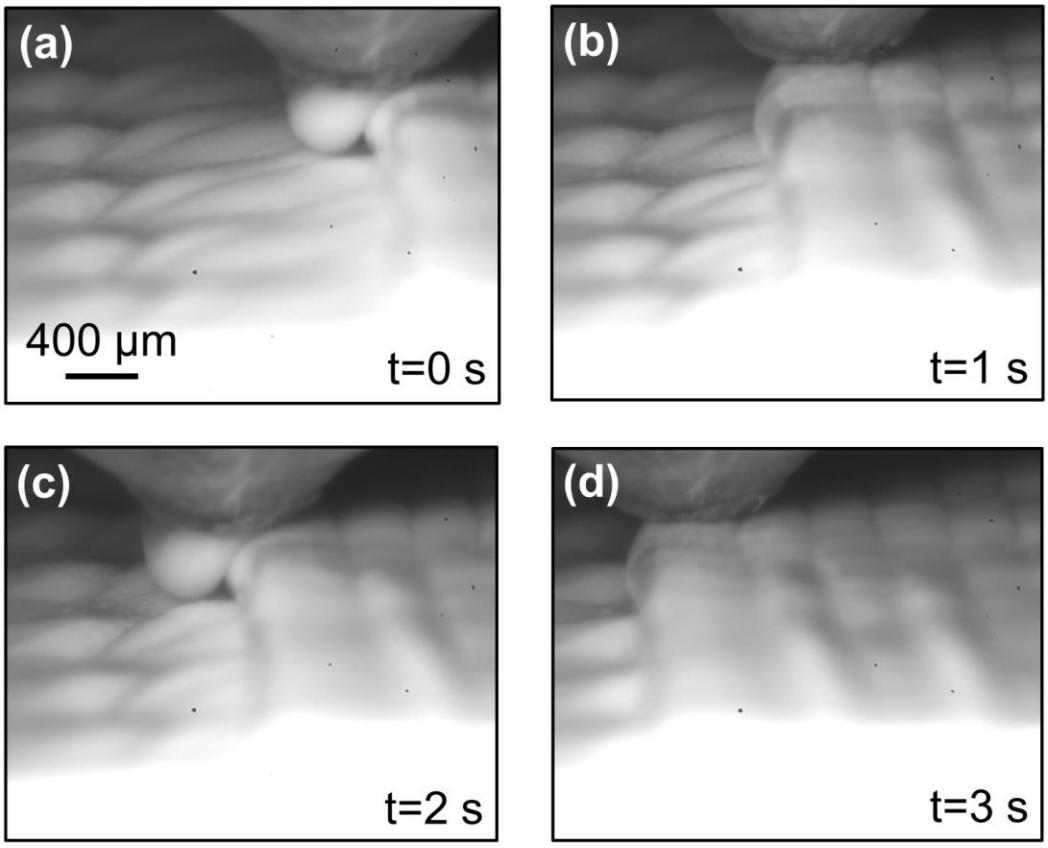

Figure 2.3. Images of the baseline 3D printing process at 6000 mm/min raster speed, 100% infill and 0.4 mm layer height. Parts (a) through (d) shows images at 1 second interval captured through the high speed camera.

2.2.2. Effect of changing infill percentage

Experiments are carried out at multiple values of the infill density between 50% and 95% while holding the raster speed constant and layer height constant at 6000 mm/min and 0.4 mm respectively. Images from these experiments are shown in Figures 2.4(a) through 2.4(d) for four different infill percentage values. These images clearly show a significant effect of the infill density on the microstructure. As expected, the polymer lines are far apart and disperse at 50% infill, and get increasingly closer to each other at larger infill percentages. As a result, a greater

infill percentage is expected to result in higher thermal conductivity due to improved adhesion as shown in Figure 2.4. This is investigated through measurement of thermal conductivity of these samples. The measured thermal conductivity, plotted in Figure 2.5 clearly increases with increasing infill percentage. This variation is found to fit well by a linear curve. Figure 2.5 also shows cross section images of printed samples obtained with a microscope digital camera for the highest and lowest infill percentage cases. The cross-section image for 50% infill indicates significant gaps between lines, which is consistent both with the corresponding *in situ* rastering image in Figure 2.4(a) as well as the low value of the measured thermal conductivity. Similar consistency is observed between the cross section for the 95% infill, which shows tight packing of lines, and corresponding *in situ* image and thermal conductivity measurements.

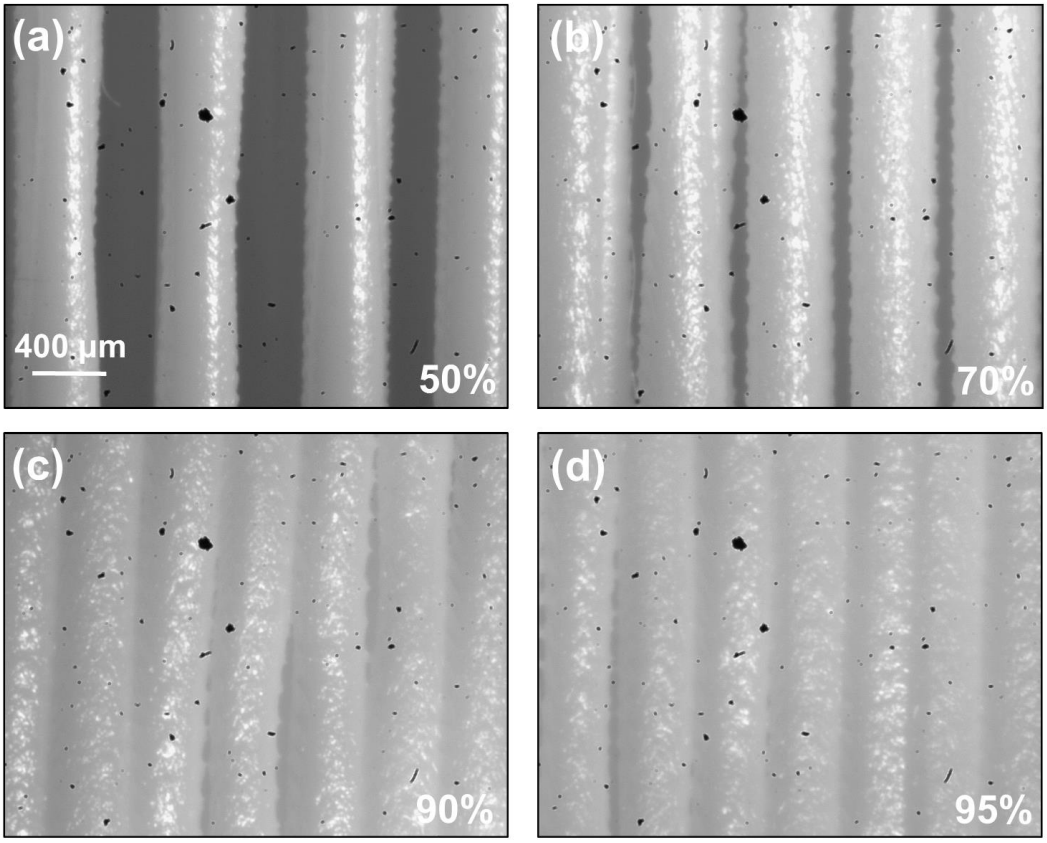

Figure 2.4. Images of the 3D printing process at different infill density values. Parts (a) through (d) show images at the end of the process for 50%, 70%, 90% and 95% infill density respectively.

These data and images clearly indicate that infill percentage plays a key role in determining thermal conductivity through its influence on the microstructure. Note that each thermal conductivity plotted in Figure 2.5, and in all subsequent figures, represent an average of measurements taken on three samples printed with the same set of parameters. A tight fit is found among these three data in each case, with the worst-case deviation of less than 3%.

The effective thermal conductivity of the sample may be modeled as a combination of the thermal conductivities of the filament material and air gap. While the exact nature of how these thermal conductivities combine may not be known, lower and upper limits for the combined thermal conductivities may be estimated from series and parallel combinations of the two thermal resistances based on the infill percentage as follows:

$$\frac{1}{k_{min}} = \frac{\varphi}{k_{air}} + \frac{1-\varphi}{k_{filament}} \tag{3}$$

and

$$k_{min} = \varphi k_{air} + (1-\varphi) k_{filament} \tag{4}$$

where φ is the infill percentage.

k_{min} and k_{max} are plotted in Figure 2.5 as functions of φ for comparison with experimental data. Figure 2.5 shows that experimentally measured thermal conductivity at each infill percentage lies between the theoretically predicted upper and lower limits. This provides a validation of the experimental measurements.

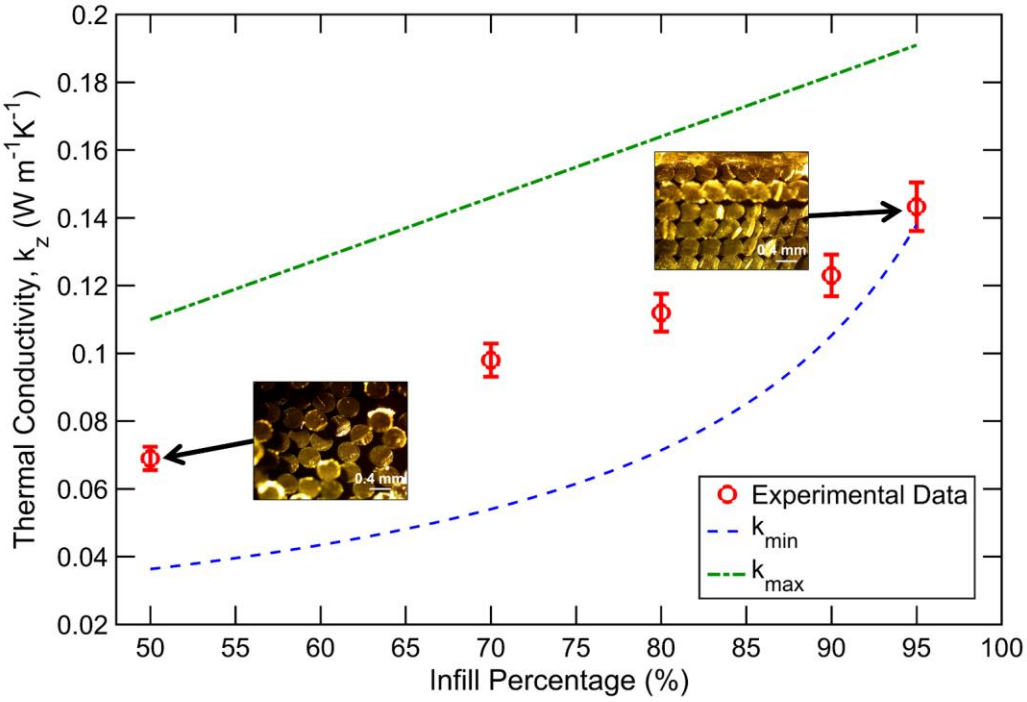

Figure 2.5. Plot showing the variation of build direction thermal conductivity with infill density. Cross section images of samples for 50% and 95% infill clearly show the impact of infill on the microstructure of the printed part. Theoretically calculated upper and lower limits based on series/parallel combination of thermal resistances are also shown for comparison with experimental data.

2.2.3. Effect of raster speed

High speed imaging and post-printing thermal conductivity measurements are carried out at four different raster speeds for a 100% infill and 0.4 mm layer height. Figure 2.6 shows high speed images of the printing process at four different times for each raster speed. These images show the effect of raster speed on the microstructure. Slow raster speed offers more time for heat transfer to the underlying and adjacent filaments, which causes these lines to remain at elevated

temperatures for greater time, and therefore merge with each other effectively. This is expected to result in improved thermal conductivity.

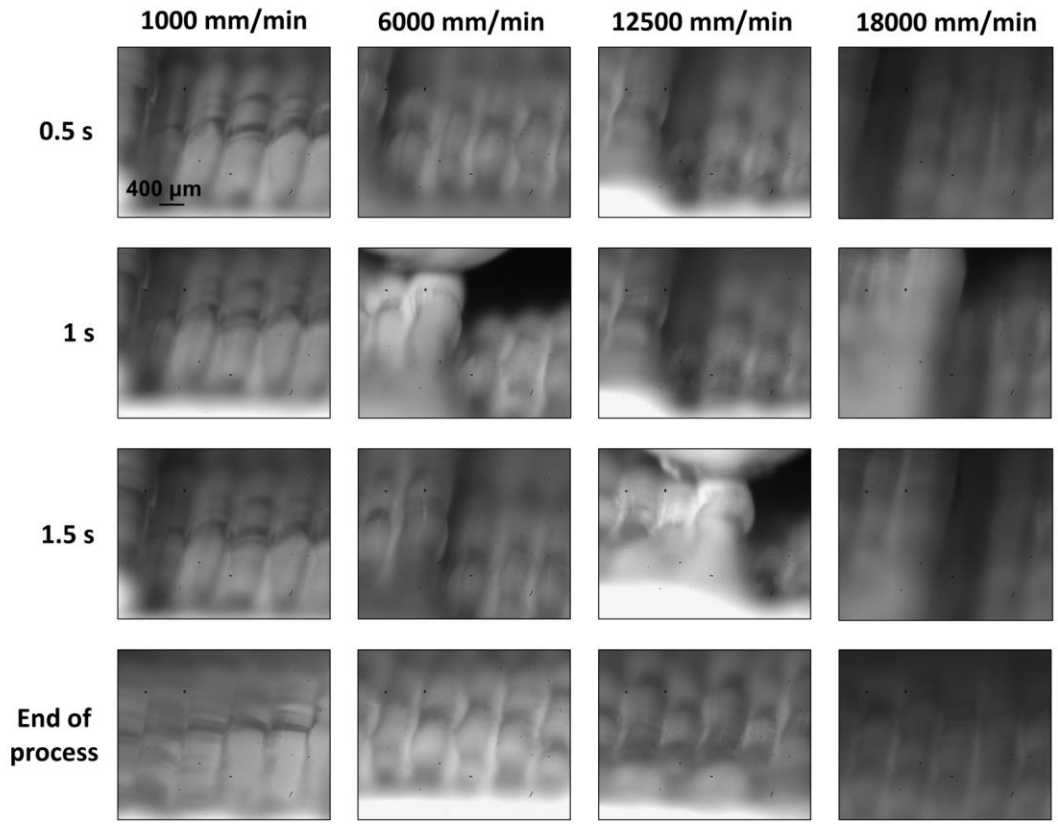

Figure 2.6. Images of the 3D printing process at different times for four different raster speeds. The change is microstructure with raster speed at the end of process results in different thermal conductivity values for different raster speeds.

On the other hand, the merging process may remain incomplete if the raster speed is too large, and heat transfer between filaments is not complete, resulting in lower thermal conductivity. In order to further investigate this, thermal conductivity of printed parts is measured for various raster speeds. Figure 2.7 shows greater thermal conductivity at lower raster speeds, which confirms the hypothesis above about the effect of raster speed on filament merging and therefore on infill. Cross-

section images of samples printed at different raster speeds, shown in Figure 2.7 are in general consistent with *in situ* imaging and corresponding thermal conductivity measurements. A comparison of these cross-section images at different raster speeds indicates better merging between filaments and greater infill at lower raster speeds, which corroborates well with measurement of higher thermal conductivity at lower raster speeds.

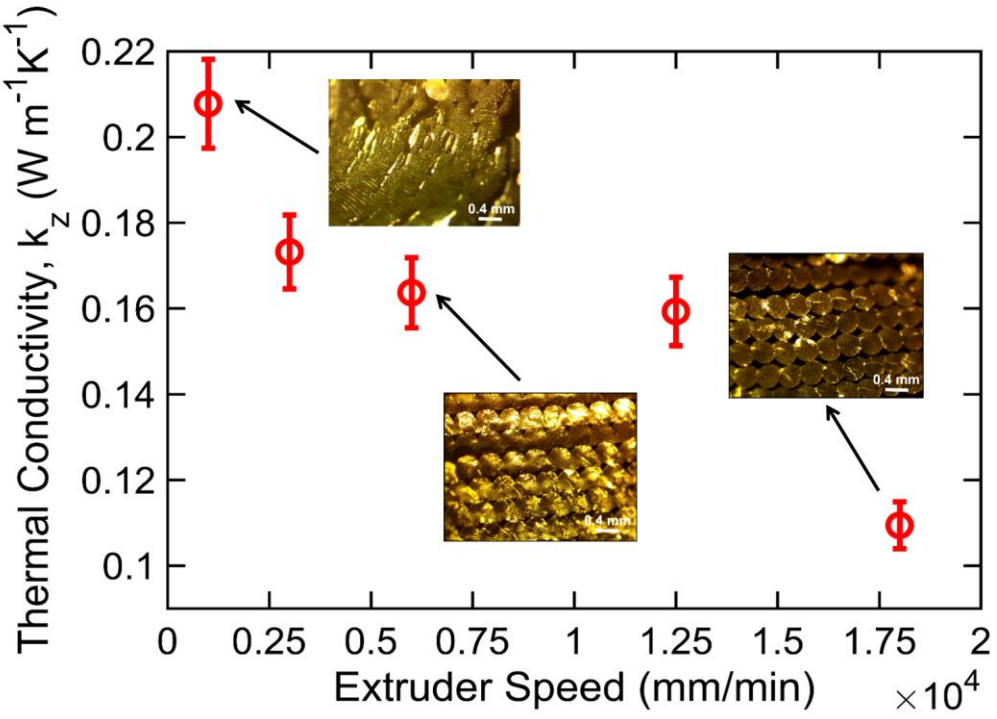

Figure 2.7. Plot showing the variation of build direction thermal conductivity with raster speed. Cross section images of samples for two cases are also shown. The measured variation agrees well with observations of the microstructure through *in situ* high speed imaging and cross-section imaging.

2.2.4. Effect of layer height

The effect of layer height on thermal conductivity is investigated. In these experiments, raster speed and infill percentage are fixed at 6000 mm/min and 100%

respectively, while layer height is varied between 0.2 mm and 2.5 mm. Measurements summarized in Figure 2.8 show that thermal conductivity increases with increasing layer height. This is because for the same overall sample size, a greater layer height results in lower number of layers, and hence a reduced number of interfaces between layers. This results in diminished contribution of inter-layer thermal contact resistance to the effective thermal conductivity. This is consistent with recent measurements and modeling that have indicated a dominant role of the thermal contact resistance in thermal conductivity of the sample [27]. The reduced number of interfaces between layers is clear from the cross-section images shown in Figure 2.8. These measurements and images confirm the dominant role of inter-layer thermal contact resistance on thermal properties.

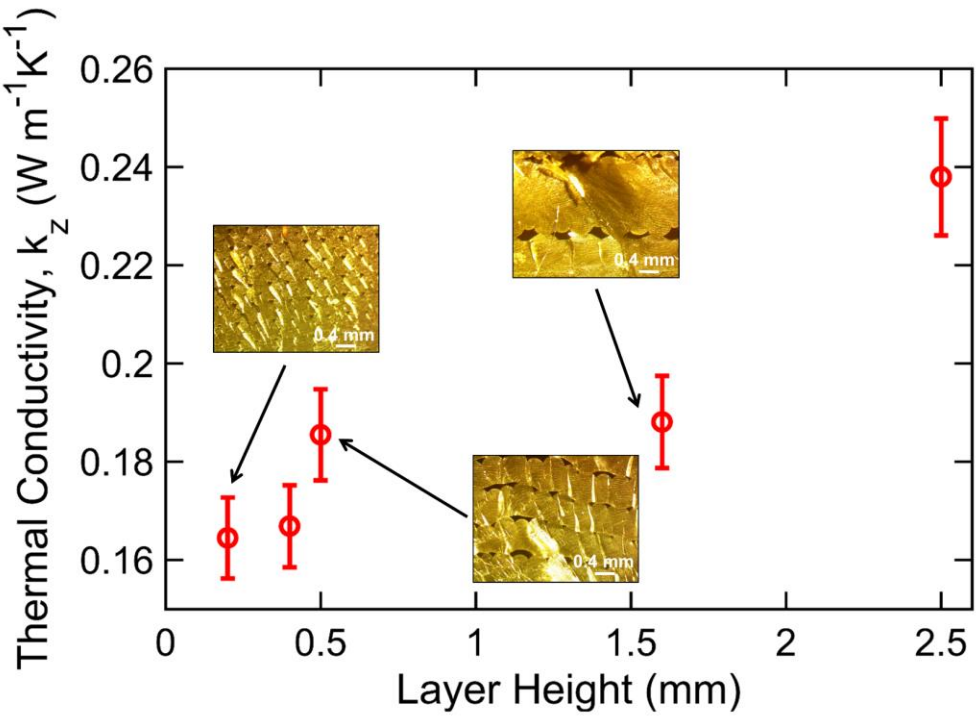

Figure 2.8. Plot showing the variation of build direction thermal conductivity with layer height for the same overall sample size. The increase in

thermal conductivity with increasing layer height clearly indicates the key role of interfacial thermal contact resistance in determining thermal conductivity in the build direction.

2.2.5. Effect of raster orientation

It is of practical relevance to understand how raster orientation impacts thermal conductivity. Raster orientation is a commonly available setting in most polymer AM platforms. In most cases, the raster orientation can be set to toggle between two angles from one layer to the next. Samples are printed for four different raster orientations - 0°/0°, 0°/90°, +20°/-20° and +45°/-45°. In the first case, raster lines in successive layers are all oriented in the same direction, while in the second case, raster lines are orthogonal to each other. In the other cases, raster lines criss-cross each other at the specified angles. Thermal conductivity of each sample is measured using the methods discussed above. Figure 2.9 shows measured thermal conductivity values for these cases, along with cross section images. These measurements indicate some dependence of thermal conductivity on raster orientation. Specifically, it is found that thermal conductivity is largest for 0°/0° and 0°/90° cases. For cases where the raster lines in successive layers are at other non-orthogonal angles (+20°/-20° and +45°/-45°), a lower value of thermal conductivity is measured. This likely occurs due to reduced contact between successive layers due to the non-orthogonal angle.

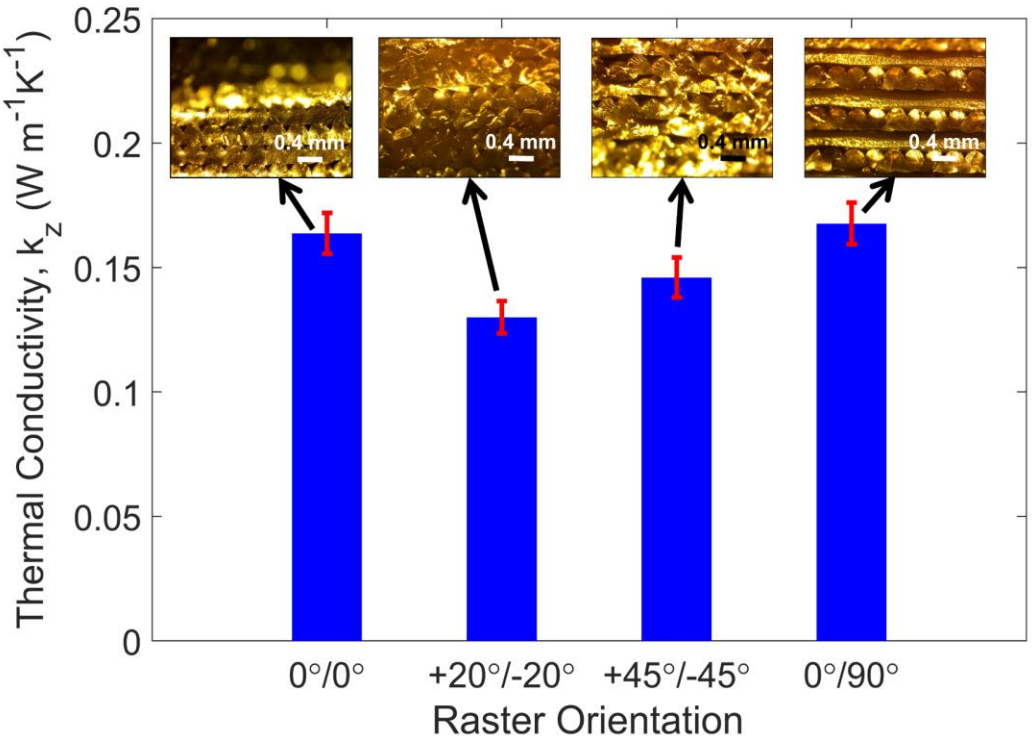

Figure 2.9. Measured build-direction thermal conductivity as a function of raster orientation

2.2.6. Discussion

The experimental measurements and imaging data discussed in sub-sections above establish a correlation between thermal conductivity of built parts and various process parameters. These data can provide critical input for determining the right process parameters for obtaining specific thermal properties of interest in the built part. Further, these data also indicate the possibility of obtaining spatially varying thermal properties by smartly changing process parameters in different parts of the build. For example, it may be possible to dynamically reduce raster speed within the feasible parameter space for manufacturability in a specific portion

of the part being built in order to obtain higher thermal conductivity only in that portion. Such a capability may result in integrated parts with unique functionality in multiple applications.

Further, several applications call for multifunctional parts, for example those that must serve both thermal and structural function. In such a case, optimization of process parameters is important from both thermal and structural perspectives. Results presented in this work, in conjunction with past reports on mechanical properties, may help drive such an optimization. In cases where high thermal conductivity is required in addition to good mechanical strength, the variations of both objectives as functions of process parameters are in general aligned with each other. For example, reducing raster speed may increase both mechanical strength and thermal conductivity. However, in other applications, there may exist a conflict between the two objectives. For example, in applications where a structural part must also provide thermal insulation, reducing the infill percentage will improve thermal insulation, as shown in this work, but will also likely result in reduced strength. A careful co-optimization of process parameters within the feasible parameter space based on results from this work may be important for resolving such trade-offs.

Finally, there also exist trade-offs between desired thermal properties and system-level process performance that this work helps resolve. For example, while reducing the raster speed has been shown to increase thermal conductivity, which may be desirable for certain applications, it will also severely reduce throughput.

Results presented here may also be useful for understanding and resolving such trade-offs.

CHAPTER 3

EXPERIMENTAL AND THEORETICAL INVESTIGATION OF HEAT TRANSFER IN PLATFORM BED DURING POLYMER EXTRUSION BASED ADDITIVE MANUFACTURING

Ravoori, D., Lowery, C., Prajapati, H., Jain, A., 'Experimental and theoretical investigation of heat transfer in platform bed during polymer extrusion based additive manufacturing,' Polymer Testing, 73, pp. 439-446, 2019.

3.1. Experiments

Experiments are carried out to measure temperature distribution along the line of filament dispense on top of a bed as the nozzle traverses along the line. The next two sub-sections describe the experimental setup and infrared camera calibration respectively.

3.1.2. Experimental setup for polymer extrusion and temperature measurement

All experiments are carried out on the open source Anet A8 3D printer platform. In contrast with other commercially available 3D printers, the Anet A8 platform facilitates the mounting of the IR camera within 4-7 cm of the nozzle path in order to capture infrared images along the raster line. In addition, this platform also facilitates changes in process parameters such as raster speed, bed temperature, etc. A 220 by 220 mm Aluminum bed is used. Filament is dispensed through a 0.4 mm brass nozzle heated by a 40W resistive heater connected to an aluminum heater block. Anet mainboard A1284 is used to control the stepper motors and power input to the heated bed as well as the nozzle heater.

Temperatures of the nozzle tip and platform bed are set at 205 °C and 60 °C respectively. In each experiment, a previously deposited Poly lactic acid (PLA) block serves as the bed for depositing a PLA filament on. In each case, a single line of filament is dispensed as the nozzle moves at fixed speed across the viewing field of the infrared camera. Raster speed is controlled via G-Code, which is processed using Simplify3D software for the specific 3D printer. The gap between PLA base

and nozzle is controlled by varying the *z* axis parameter in the G-Code. Raster speed is confirmed through an independent measurement based on the length of filament dispensed in a fixed time interval. This calculation of the raster speed is found to be consistent with the speed set in the G-Code.

Temperature distribution in the entire field of view of the camera is captured in each experiment at a rate of 30 frames per second, following which, temperature data along the raster line are extracted.

Figure 3.1(a) shows a picture of this experimental setup. A zoom-in image of the experiment is shown in Figure 3.1(b).

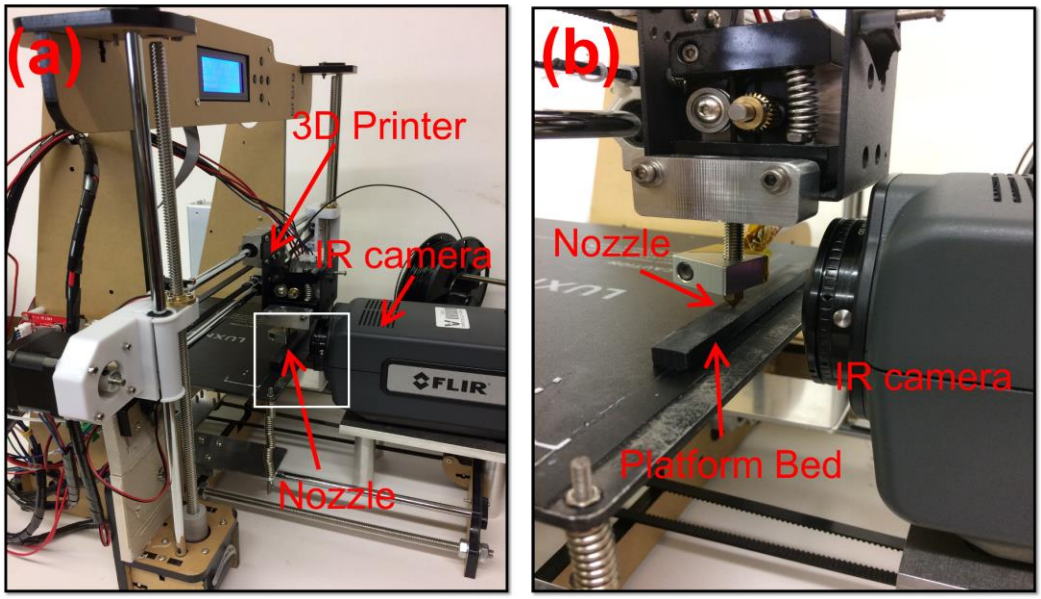

Figure 3.1. (a) Picture of the experimental setup for infrared thermography during filament rastering process in polymer-based additive manufacturing (AM), showing various AM platform components and IR camera; (b) Zoom-in of the experimental setup.

3.1.2. Infrared camera calibration

While the infrared camera offers a convenient, non-invasive mechanism for temperature field measurement, a rigorous, pre-experiment calibration is essential to ensure accuracy. A thin part of thickness 0.4 mm printed from the same PLA material used in all other experiments is placed on a temperature-controlled Instec HCS622V stage. A FLIR A6703 3.0-5.0 μm InSb infrared camera is used. Temperature of the stage is changed from room temperature to about 220 °C in 20 °C intervals. At each temperature point, the temperature of the top surface of the thin part is measured by a T-type thermocouple as well as the infrared camera. Temperature is allowed to stabilize over 20 minutes at each point prior to measurement.

3.2. Analytical Modeling

From a heat transfer perspective, the process of rastering of the filament on the bed can be represented by a heat source moving along the raster line. Solutions for the temperature distribution for such moving heat source problems already exist [44,44] and have been applied for other engineering problems such as welding and laser cutting [45,46]. This section briefly summarizes the key results of this model and then applies it to the problem of determining temperature distribution in polymer dispense based additive manufacturing, with the primary goal of predicting temperature distribution on the surface of the bed, since this directly impacts the extent and quality of bonding between adjacent filaments.

Figure 3.2 shows a schematic of the filament deposition process and subsequent thermal diffusion into the bed, which may comprise of already printed layers, or the underlying build plate on which the part is built. The filament is assumed to be deposited by a nozzle moving at a constant speed u_x along the x axis on the z=0 face of the bed, which is assumed to be thermally semi-infinite, which is justified due to the short penetration depth expected within the short time duration in which a filament is deposited. Figure 3.2 also shows a coordinate system attached to the moving nozzle, in which the coordinate ξ is given by $\xi = (x - u_x t)$. Mass of the filament deposited on the bed is assumed to be negligible compared to the bed mass, so that the only effect of filament dispense is the deposition of thermal energy $\dot{q}$ on the bed face, which then diffuses into the bed. $\dot{q}$ represents the rate at which thermal energy is deposited on the bed along with the filament material. This energy originates from the temperature of the deposited filament, the rate of deposition and heat capacity of the filament material as follows:

$$\dot{q} = \int_{T_0}^{T_n} \dot{m} C_p \, dT \tag{5}$$

where the mass flow rate $\dot{m} = \rho A V$ can be determined from the nozzle cross section area A, filament speed V and filament density ρ. Also note that C_p is the filament heat capacity, and T_n and T_0 represent the nozzle and initial bed temperatures respectively. Equation (5) includes latent energy associated with glass transition that usually occurs at a temperature between T_0 and T_n.

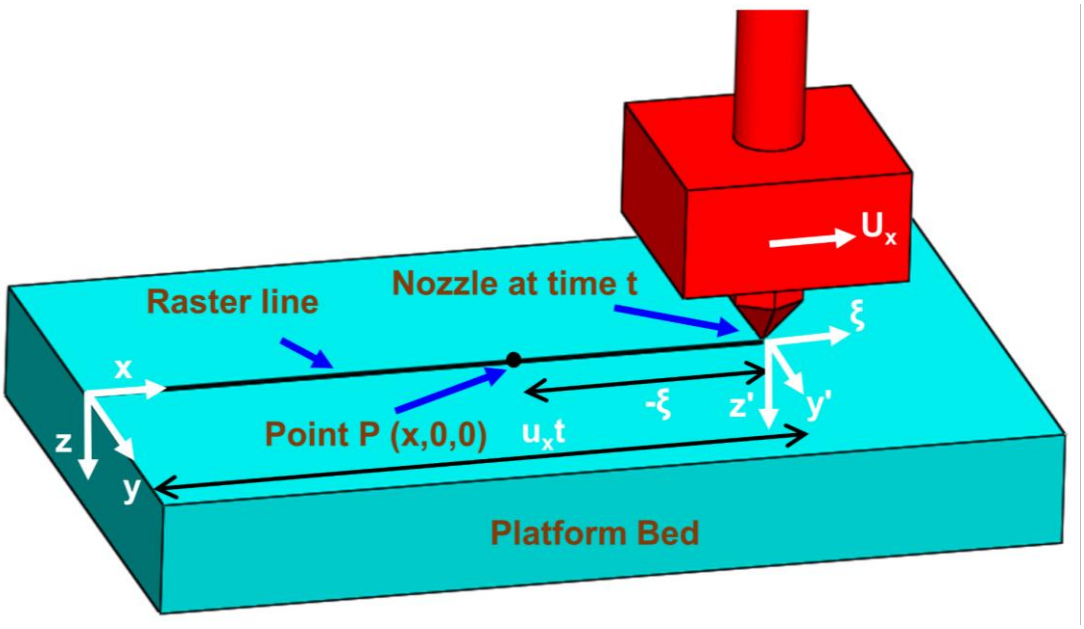

Figure 3.2. Schematic of the filament rastering process, showing one-dimensional motion of the nozzle across the bed. The coordinate axes used in the analytical model are also shown for reference. (Adapted from [44])

Assuming isotropic heat transfer in the bed, temperature-independent thermal conductivity k and thermal diffusivity α, and no internal heat generation in the bed, the governing energy conservation equation for temperature distribution in the bed $T(x,y,z,t)$ is given by

$$\frac{\partial^2 T}{\partial x^2} + \frac{\partial^2 T}{\partial y^2} + \frac{\partial^2 T}{\partial z^2} = \frac{1}{\alpha}\frac{dT}{dt} \tag{6}$$

Assuming a thermally semi-infinite bed, boundary conditions associated with equation (6) are

$$\frac{\partial T}{\partial y} \to 0 \quad as\ y \to \pm\infty \tag{7}$$

and

$$\frac{\partial T}{\partial z} \to 0 \quad as\ z \to \pm\infty \tag{8}$$

In addition, the total heat flux out of an infinitesimal sphere of radius *r* drawn around the dispensed filament must equal $\dot{q}$

$$\lim_{r\to 0}\left[-4\pi r^2 \cdot k \cdot \frac{\partial T}{\partial r}\right] = \dot{q} \tag{9}$$

where $r = \sqrt{(x-u_x t)^2 + y^2 + z^2}$ is the radial distance from the filament location in the coordinate system attached to the moving nozzle.

Using coordinate system transformation, a solution for equations (2)-(5) has been shown to be [44]

$$T = T_o + \frac{\dot{q}}{2\pi k r} exp\left[-\frac{u_x(r+\xi)}{2\alpha}\right] \tag{10}$$

Complete details of the derivation of equation (6) may be found in [44].

In the case of filament rastering on the bed, the interest is specifically on temperature distribution on the top surface, *z*=0. Also, along the line of filament dispense, the value of *y* is zero, as shown in Figure 3.2. Therefore, along the raster line, equation (10) can be simplified to

$$T = T_o + \frac{\dot{q}}{2\pi k \cdot |x-u_x t|} exp\left[-\frac{u_x(|x-u_x t| + x - u_x t)}{2\alpha}\right] \tag{11}$$

This shows that at any given point *(x,0,0)* as shown in Figure 3.2, prior to nozzle arrival, i.e. $t < \frac{x}{u_x}$, temperature is given by

$$T = T_o + \frac{\dot{q}}{2\pi k \cdot |x - u_x t|} exp\left[-\frac{u_x(x - u_x t)}{\alpha}\right] \tag{12}$$

and after the nozzle has passed over the point, temperature is given by

$$T = T_o + \frac{\dot{q}}{2\pi k \cdot |x - u_x t|} \tag{13}$$

Note that $|x|$ refers to the absolute value of x. Equation (12) indicates a very slow rise in temperature when the nozzle is somewhat far during its approach towards the point, followed by a sharp exponential increase when the nozzle is close by. Afterwards, once the nozzle has passed over the point, equation (13) predicts a gradual reduction in temperature.

In addition to the bed surface, equation (10) is also capable of predicting temperature distribution as a function of depth inside the bed. As an illustration of this, Figure 3.3 plots the temperature distribution in a cross-section of the bed at three different times as the nozzle tip rasters across the top of the bed at 3.2 mm/s speed. Figure 3.3 shows very high temperature near the nozzle tip location in each case and a rapid reduction in temperature before and after. The heat-affected zone moves along with the nozzle tip as it traverses across the bed, with some residual temperature rise downstream of the nozzle. Most of the temperature rise is limited to a shallow depth in the bed comprising just a few previously built layers, which

is consistent with experimental observations from past papers [38,42], and occurs due to the short thermal penetration depth in the small time over which a filament is deposited. Note that Figure 3.3 only accounts for temperature rise due to thermal energy deposited on the bed. Temperature rise may also occur due to other effects, such as heat transfer from the hot nozzle tip, which is further discussed in Section 3.3.

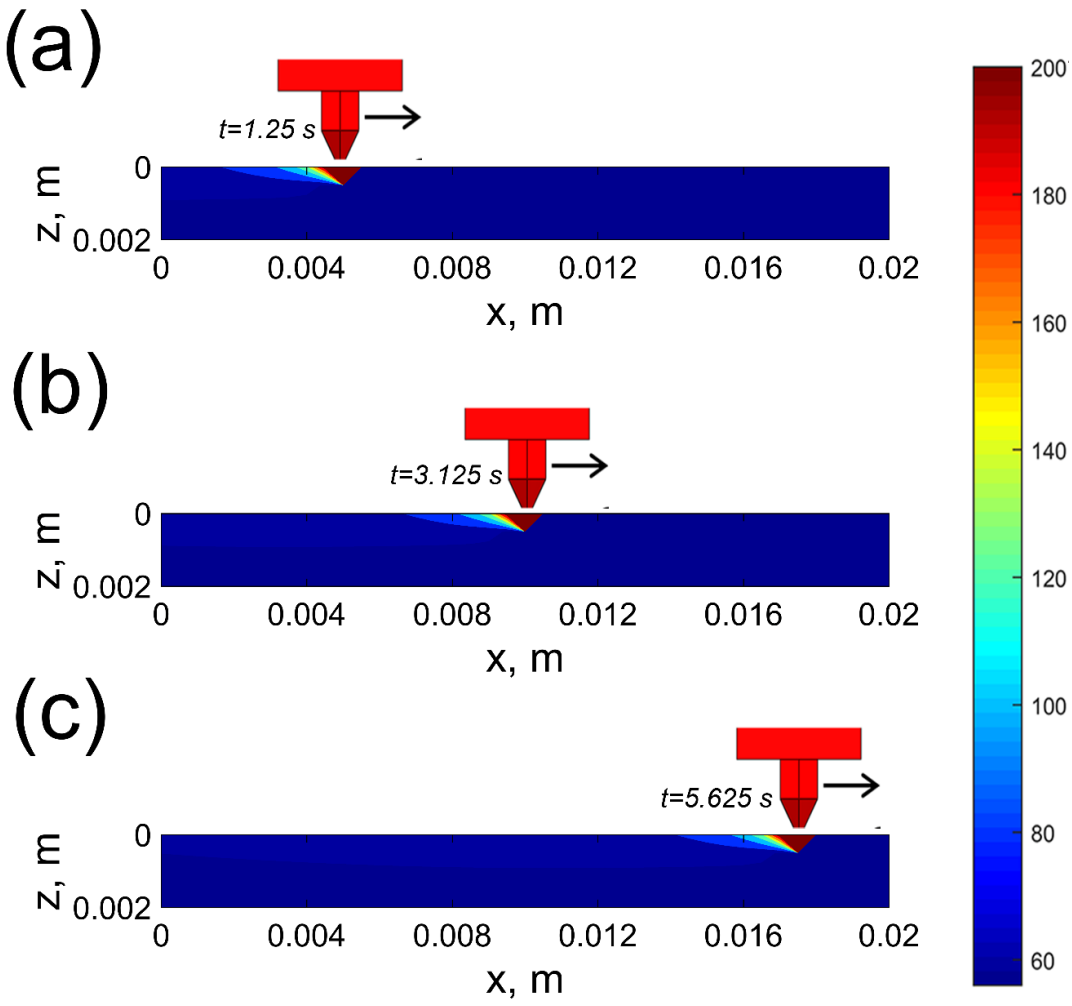

Figure 3.3. Colorplot of temperature distribution in the platform bed during the rastering of the nozzle at a 3.2 mm/s speed, based on analytical model for

diffusion of thermal energy deposited by the hot filament. Colorplots are shown at three successive times.

3.3. Results and discussion

3.3.1. Calibration of infrared thermography

Figure 3.4 shows a calibration of the infrared camera used in this work for temperature measurement. As described in section 2, temperature of the top surface of a printed PLA sample is measured both through a T-type thermocouple in direct contact with the surface as well as the infrared camera at a number of temperatures in the 75 °C to 210 °C range of interest. A value of 0.92 is used for the emissivity of PLA in the wavelength range detected by the infrared camera. Figure 3.4 plots temperature measured by the infrared camera against thermocouple measurement at a number of temperature points, showing good agreement over the entire temperature range of interest. All points lie close to the ideal 45° line. This establishes the accuracy of the infrared thermometry approach for temperature measurement utilized in all measurements in this work.

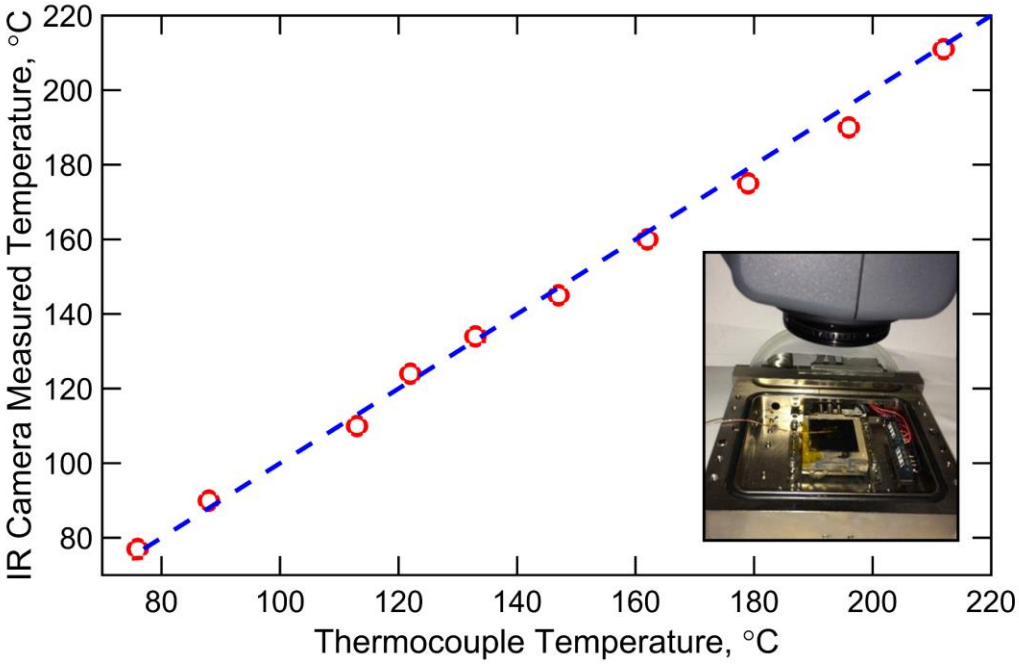

Figure 3.4. Comparison of temperature of the top surface of a PLA block measured by infrared camera with direct thermocouple measurement over the temperature range of interest. An emissivity value of 0.92 for the infrared camera results in excellent agreement between the two. Inset in the figure shows a picture of the experimental setup for calibration.

3.3.2. Effect of raster speed on temperature distribution

A number of experiments are carried out to measure temperature distribution on the platform bed along the raster line. In each case, the temperature field is recorded as a function of time at a rate of 30 frames per second, so that transient variations in the temperature field can be captured. At a fixed point on the line, as the nozzle tip approaches the point, temperature is expected to go up. When the nozzle is directly above the point of interest, the temperature is expected to be the highest, and then decay as the nozzle moves away. The nature of temperature rise prior to nozzle arrival as well as decay afterwards are both very important for understanding filament-to-filament merging and bonding. Infrared thermography

of the filament dispensing process is carried out in a number of process conditions. As an example, Figures 3.5(a)-(c) show infrared thermographs captured at three different times for a dispense process at 2.7 mm/s raster speed. In these images, the nozzle tip moves from left to right. The temperature distribution along the raster line can be clearly seen in these images. The peak temperature occurs directly under the nozzle tip and moves from left to right along with the nozzle tip. In each case, temperature distribution as a function of space and time can be extracted quantitatively from the infrared thermographs such as Figures 3.5(a)-(c).

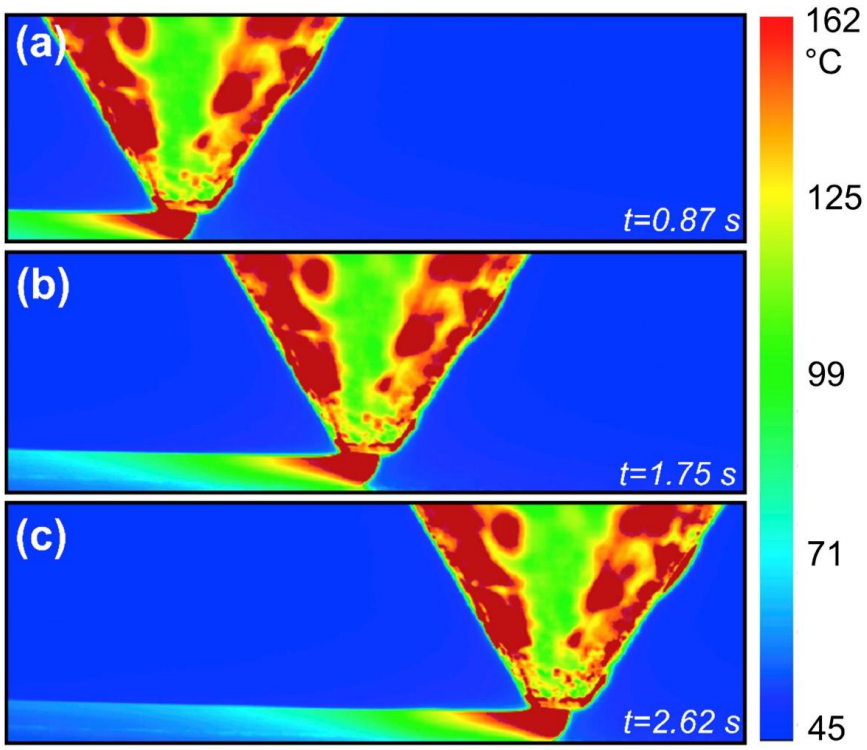

Figure 3.5. Infrared thermographs obtained at three different times for rastering of a single line wherein the nozzle moves from left to right at 2.7 mm/s speed.

To further illustrate the temperature measurement approach, the effect of raster speed on temperature distribution is examined. Figure 3.6(a) plots

temperature as a function of time at a fixed point *A* along the raster line for three different raster speeds. These measurements show that the peak temperature reached at point *A* is invariant with raster speed. However, as expected, the time at which the peak temperature occurs changes with raster speed, occurring later at lower raster speeds. At each raster speed, temperature rises slowly as the filament front approaches the point of interest. An inflexion in the measured temperature is observed when the filament front is around 3.5 mm away from the point of interest, leading to very sharp increase in temperature until the peak corresponding to the arrival of the nozzle tip directly above the point of interest. While the measured temperature is expected to rise as the nozzle tip approaches, the inflexion in temperature, observed consistently in all experiments indicates that temperature rise at the point of interest may be influenced by another heat source in addition to diffusion of thermal energy deposited by the dispensed filament.

These measurements are repeated for two additional points – *B* and *C* – as shown in the insets of Figures 3.6(b) and 3.6(c). Points *B* and *C* are further downstream of point *A*. Figures 3.6(b) and 3.6(c) show, as expected that the time at which temperature peak occurs at these points is later than in the case of point *A*. The shapes of temperature curves, including the inflexion point as well as the peak temperature value in Figures 3.6(b) and 3.6(c) are all consistent with Figure 3.6(a). Peak temperature is nearly the same at each point, which is consistent with the semi-infinite nature of the bed in the short time duration of these experiments.

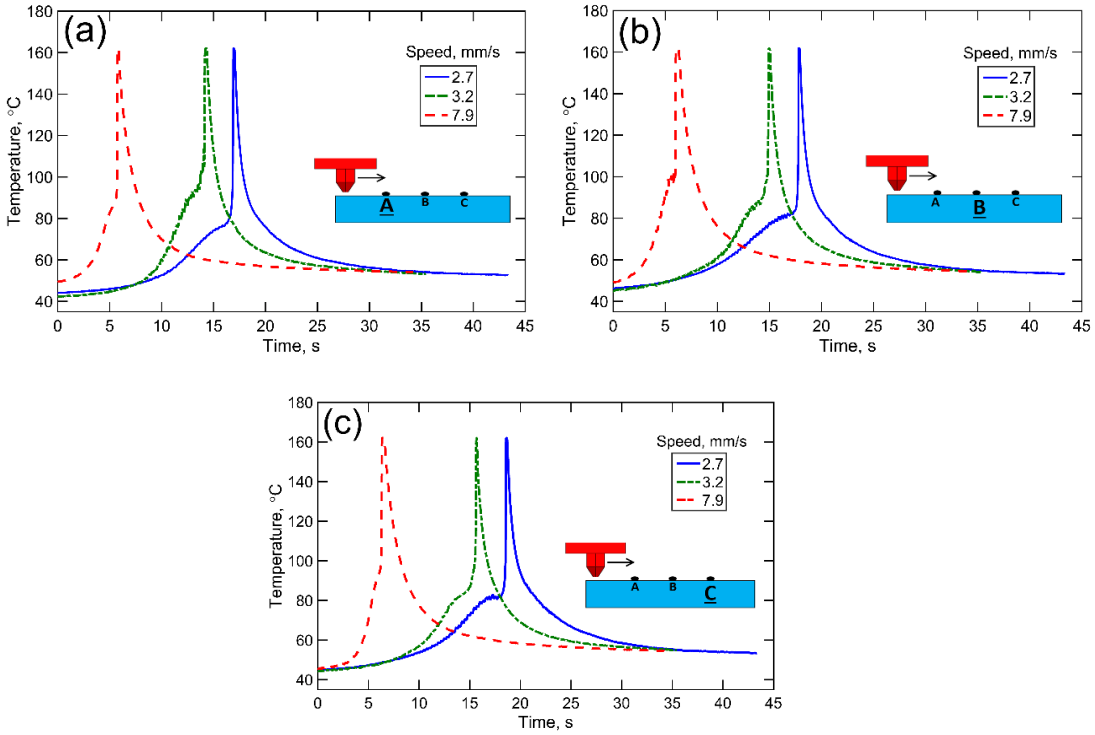

Figure 3.6. Measured temperature as a function of time at a fixed location along the raster line for three different raster speeds. (a)-(c) present these data for three distinct points *A*, *B* and *C* along the raster line as shown in the inset schematics.

3.3.2. Contributions of filament dispensing and hot nozzle tip towards temperature rise

As discussed in Section 3, diffusion of thermal energy deposited along with the dispensing filament into the bed causes temperature rise. Further, thermal conduction from the nozzle tip may also play a role due to the close proximity of the nozzle tip.

In order to investigate these factors that affect temperature rise and its variation with time, temperature at a specific point *A* along the filament dispense line is measured at a raster speed of 2.7 mm/s. These measurements, carried out

with and without filament dispensing out of the nozzle tip, are plotted in Figure 3.7. The nozzle tip is at 205 °C in both experiments and the gap between nozzle tip and bed is 0.4 mm. Clearly, data from the experiment without filament dispense corresponds to the contribution of thermal conduction from the hot nozzle tip alone, since hot filament is not being dispensed on the bed. On the other hand, data from the experiment with filament dispense is the sum total of contributions from both thermal energy deposited along with filament and heat transfer from the hot nozzle tip. Due to the linearity of heat transfer in this problem, contributions from these two sources are expected to add up linearly. Therefore, the difference between experimental data in the two cases represents the effect of thermal energy deposited along with the filament, which is also plotted in Figure 3.7. In this manner, these two experiments clearly separate out the contributions of both sources of temperature rise. Figure 3.7 shows that thermal energy deposited along with the filament has negligible effect on temperature rise on the bed until the nozzle is very close to the point of interest, beyond which, the temperature rises very rapidly and then decays away once the nozzle has passed. This behavior is representative of typical predictions from moving heat source theory. On the other hand, temperature rise due to heat transfer from the hot nozzle increases faster during approach of the nozzle towards the point of interest, but does not peak as dramatically as the contribution from the hot filament dispense. Temperature rise due to heat transfer from the hot nozzle occurs primarily due to thermal conduction and radiation across the small gap between nozzle and bed.

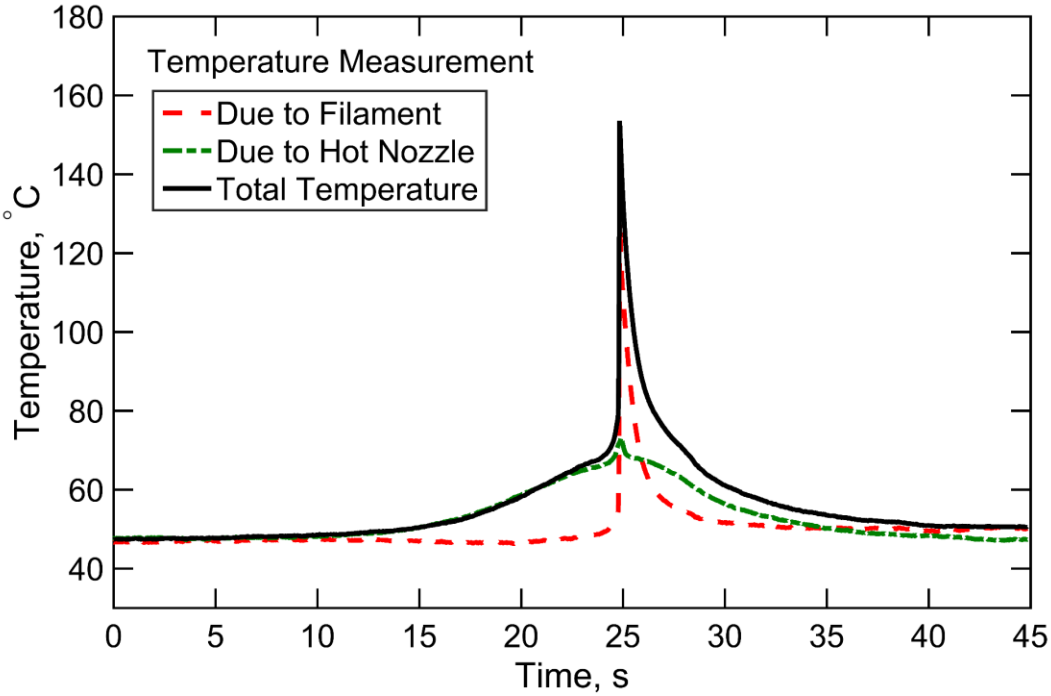

Figure 3.7. Plot of the contributions from energy deposition by hot filament dispense and thermal conduction from hot nozzle tip towards temperature at a point on the platform bed. Sum total of the two contributions is also shown.

The large size of the hot nozzle compared to the filament diameter explains why temperature rise due to the hot nozzle is spread out over a larger time interval compared to temperature rise due to the filament. The experiment without filament dispense also explains the inflexion point observed in Figure 3.6 – it occurs due to the arrival of the hot nozzle block above the point of interest before the actual dispensing of the filament on the bed.

To further validate this, the difference between experimental data with and without filament dispense, which represents the temperature rise only due to thermal energy deposited along with the filament is compared against predictions from the moving heat source theory, which accounts for heat diffusion from the

dispensed filament into the bed. Figure 3.8(a) shows very good agreement between the two. As discussed in section 2, due to the presence of a singularity at $t=x/u_{x,}$ moving heat sources theory predicts infinite temperature when the nozzle tip is precisely at the point of interest. This may restrict comparison of theoretical predictions with experimental at exactly that time. However, it accurately tracks measured temperature both before and after nozzle arrival, as shown in Figure 3.8. In particular, the decay of temperature at the point of interest after the nozzle has passed is important for determining the quality of bonding at that point with neighboring filaments. The model correctly captures this transient, as shown in Figure 3.8.

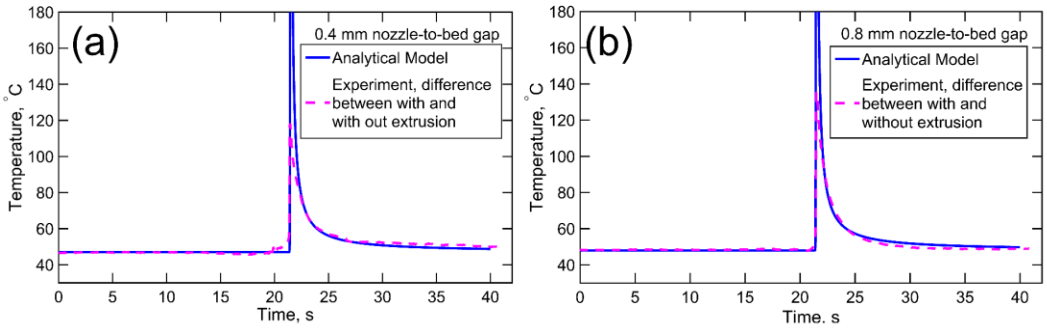

Figure 3.8. Comparison of the effect of thermal conduction from hot nozzle tip with prediction from moving heat source theory for 0.4 mm and 0.8 mm nozzle-to-bed gap.

The contribution from the dispensed filament does not lead to significant temperature rise until the nozzle tip is very close to the point of interest, at which time, temperature rises extremely fast. This is consistent with moving heat source theory that predicts flat temperature at early times followed by a sharp increase in

temperature just prior to nozzle arrival at the point of interest, as shown in equation (8).

Data presented in Figures 3.7 and 3.8 not only identify and quantify the relative contributions of the two sources of temperature rise, but also validate the measurements through good agreement with an analytical model. The key role played by heat transfer from the hot nozzle through the standoff gap is particularly interesting and not necessarily intuitive.

The influence of heat transfer from the nozzle tip on temperature rise in the bed is investigated further through experiments at two different values of the gap between the nozzle tip and bed. Figure 3.9 plots the temperature component at a fixed point due to heat transfer from the hot nozzle tip, determined from experiments without filament dispense at two different gaps. These data clearly show a reduction in temperature rise due to the hot nozzle when the gap is increased, further confirming the important role of heat transfer from the nozzle tip. Heat transfer between the two bodies is expected to reduce with increasing gap, as shown in these experimental data. The small bumps in the curves in Figure 3.9 correspond to the time of arrival of the nozzle body above the point of interest. Further, Figure 3.8(b) plots temperature rise due to thermal energy deposited along with filament for 0.8 mm gap and compares against predictions from moving heat source theory. Similar to the 0.4 mm gap case shown in Figure 3.8(a), there is good agreement in this case as well, further validating the experimental approach for understanding

the contributions from the two sources on temperature rise in the platform bed and the role of the nozzle-to-bed gap on temperature rise.

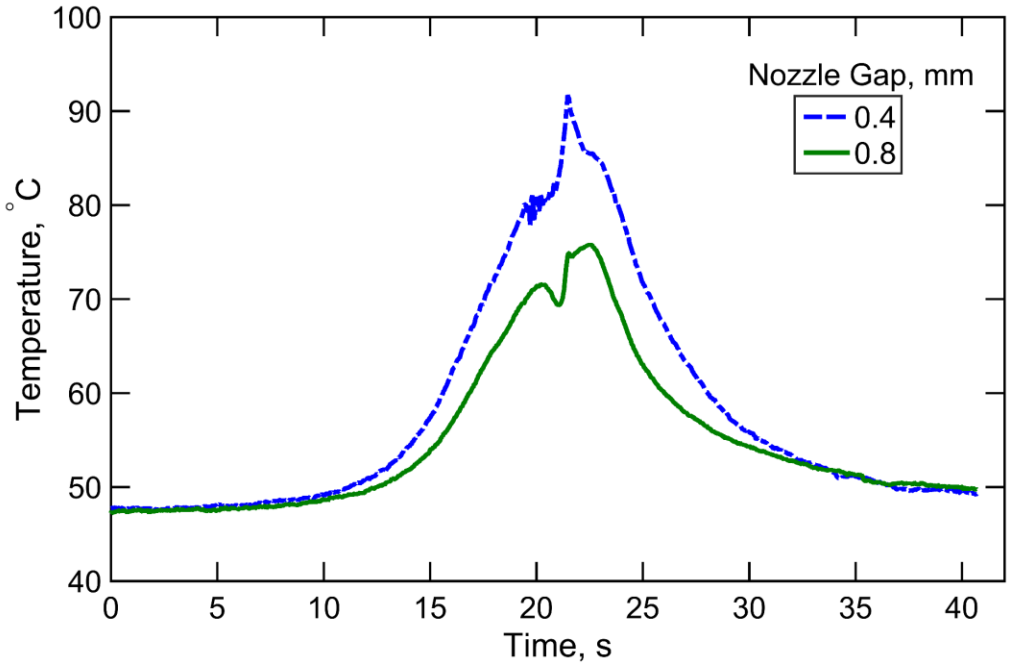

Figure 3.9. Temperature due to thermal conduction from hot nozzle tip at a point on the raster line as a function of time for two different nozzle-to-bed gaps.

3.3.3. Temperature decay in the filament after completion of dispense process

In addition to understanding temperature rise during the process of dispensing a filament line, the process of temperature decay in the line after completion of the dispense process is also important. For example, once a line has been dispensed, the nozzle tip typically moves over and dispenses the adjacent filament line. Merging of the two adjacent lines is critical for ensuring good mechanical strength of the built part. This process is driven primarily by the temperature history of the two merging filaments that must be kept at above glass transition temperature for as long as possible. In light of this, measurements are

carried out to quantify the nature of temperature decay in the filament line after completion of the rastering process. Figure 3.10 plots temperature as a function of time at three different points *A*, *B* and *C* on the filament line after completion of the filament dispense process. In this case, the line is printed from left to right at 3.2 mm/s speed, and point *C* is closest to the end point of the line, as shown in the inset in Figure 3.10. Experimental data show that point *C* is initially the hottest among the three points considered. Temperature at each point decays smoothly and becomes uniform after about eight seconds. Figure 3.11 plots the entire temperature distribution along the filament line at multiple times. As expected, Figure 3.11 shows an asymmetry in the temperature distribution at t=0 s, since the far end of the line has been dispensed more recently than the end near x=0. As the line cools down, temperature reduces everywhere along the line, while also becoming more thermally uniform. Quantitative measurement of temperature evolution along the line shown in Figure 3.11 is critical because temperature at any point along the line influences the extent of bonding with the adjacent line, which is usually printed immediately afterwards while the first line is thermally decaying. Curves in Figures 3.10 and 3.11 may be useful for optimizing the process parameters in order to ensure better and spatially uniform merging between filaments.

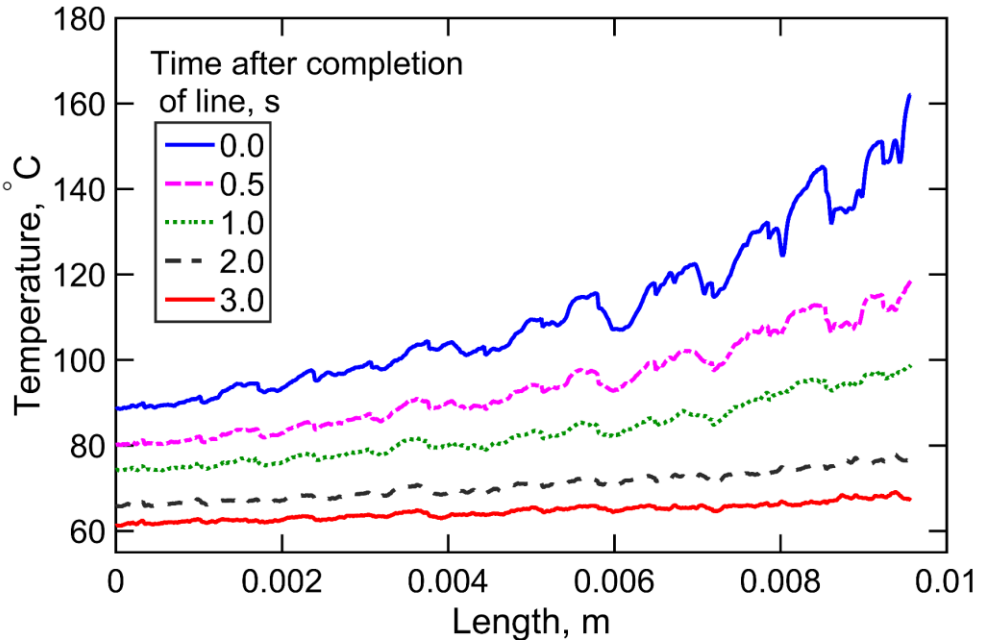

Figure 3.11. Temperature of the entire raster line at multiple times after completion of the raster process.

CHAPTER 4

NOZZLE-INTEGRATED PRE-DEPOSITION AND POST-DEPOSITION HEATING OF PREVIOUSLY DEPOSITED LAYERS IN POLYMER EXTRUSION BASED ADDITIVE MANUFACTURING

Ravoori, D., Prajapati, H., Talluru, V., Adnan, A., Jain, A., 'Nozzle-integrated pre-deposition and post-deposition heating of previously deposited layers in polymer extrusion based additive manufacturing,' *Additive Manufacturing*, **28**, pp. 719-726, 2019.

4.1 Experiments

Experiments are carried out to measure the thermal effect of preheating and postheating configurations during filament dispensing process. Temperature along the raster line is measured as a function of time using an infrared camera. Figure 4.2(a) and 4.2(b) show pictures of the experimental setup, comprising a custom-built Anet A8 3D printer, a FLIR A6703sc InSb infrared camera and a 6 mm thick poly-lactic acid (PLA) sample on which filaments are deposited. The Aluminum build plate dimensions are 200 mm by 200 mm. Stepper motors for x, y and z movement are controlled by an A-1284 mainboard. The geometry to be printed is modeled in a CAD software and converted to G-code using Simplify3D software. 1.75 mm diameter TrueBlack color PLA filament from Makerbot is fed into the nozzle block, heated up and dispensed through a 0.4 mm brass nozzle. Filament feedrate is determined by Simplify3D software based on process parameters such as print speed and layer height in order to maintain consistent flowrate.

The standard metal heater block surrounding the nozzle is replaced with a custom-built metal heater block containing the additional preheater element. An Aluminum block is machined and integrated with the nozzle assembly in order to obtain the preheater/postheater configuration, as shown in the schematic and picture in Figures 4.1(a) and 4.1(b) respectively. A threaded hole is drilled in the metal block in order to accommodate the nozzle assembly, which contains an embedded 40W cartridge heater and a thermistor for temperature measurement. Thermistor reading is used by the A1284 mainboard to control the heating current

going into the heater in order to maintain the same temperature in the nozzle block as well as preheater block. Due to the high thermal conductivity of aluminum, the entire block is expected to be at the set temperature, which is validated through temperature measurement using an external thermocouple at the start of experiments. All experiments are carried out at a nozzle/heater block temperature of 205 $^{\circ}$C. The metal block is 30 mm in length. The bottom surface of the preheater block is located just above the nozzle tip. Two different preheater samples with gaps of 0.6 mm and 1.6 mm between the bottom surface of the preheater block and nozzle tip are built. The nozzle tip is always placed 0.35 mm above the surface on which filament is dispensed, so that the bottom surface of the preheater block is 0.95 mm and 1.95 mm above the surface for the two preheater samples respectively.

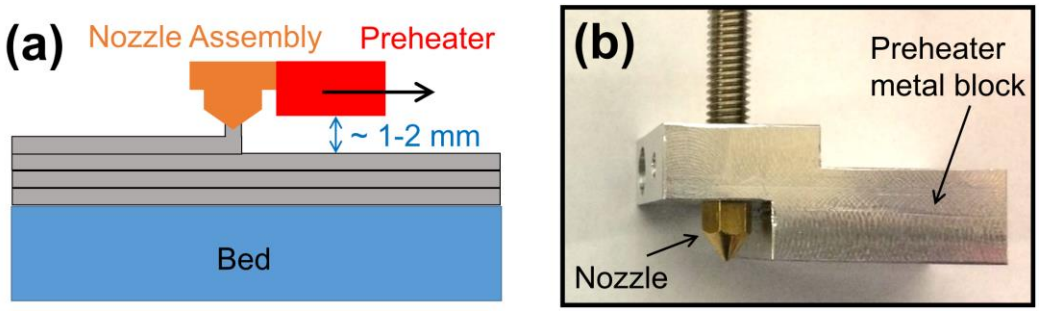

Figure 4.1. (a) Schematic of nozzle-integrated hot surface based preheating. Note the raster direction. If reversed, the preheater effectively acts as a postheater. Not to scale. (b) Picture of preheater integrated with the dispensing nozzle.

Note that when the nozzle-heater assembly shown in Figures 4.1(a) and 4.1(b) moves from left to right while dispensing filament, the metal block moves ahead of the dispensing nozzle, and therefore acts as a preheater. On the other hand, nozzle motion from right to left results in the block acting as a postheater that heats

up the filament after dispense. In addition, a combined pre/post-heater is also fabricated by bolting together two separately machined Aluminum parts. This allows simultaneous heating both before and after filament dispense.

A 6 mm PLA block is printed using the process described above with both preheating and postheating configurations. For reference, a baseline process using only the conventional nozzle assembly is also carried out. Experiments are carried out at multiple print speeds of 2.7, 4.1, 10.4 and 21.6 mm/s for both 0.95 mm and 1.95 mm gap configurations. In each case, the nozzle and heater are maintained at 205 °C through Joule heating provided by a 40 W heater.

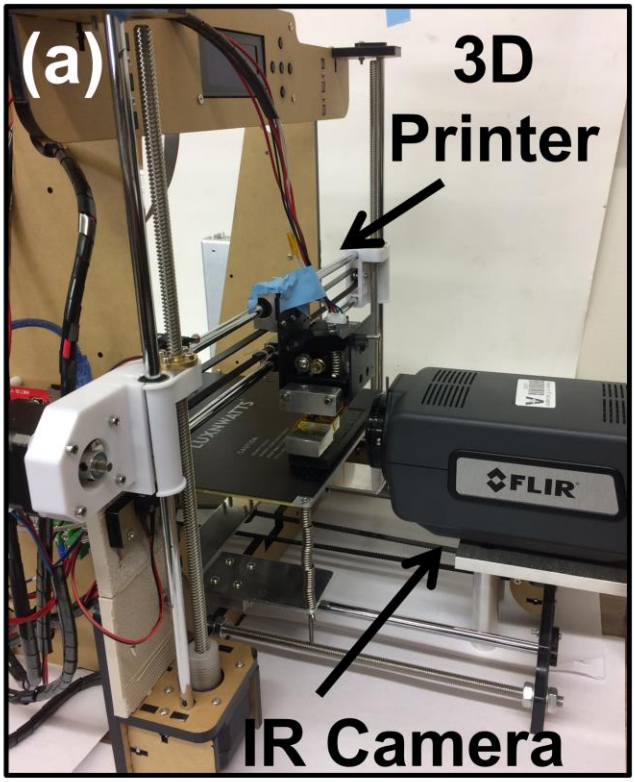

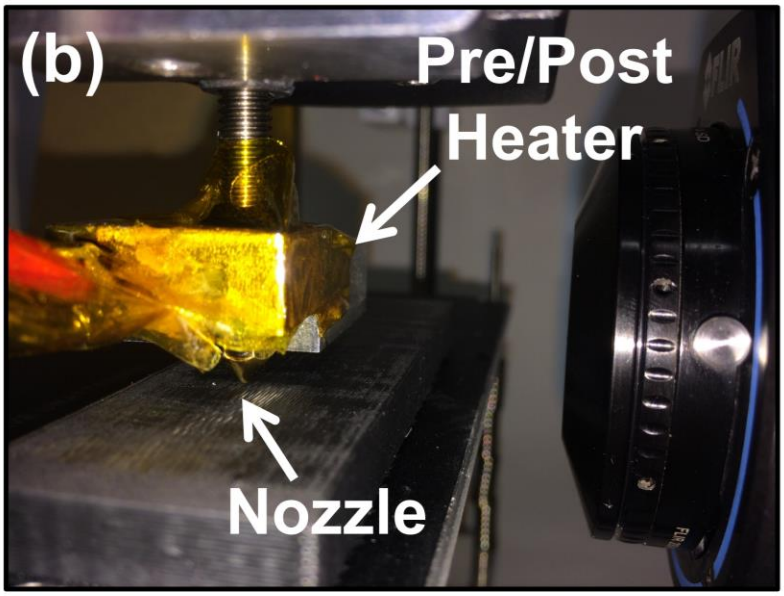

Figure 4.2. (a) Picture of the experimental setup, (b) Zoom-in showing the nozzle, preheater and IR camera lens.

The infrared camera in these experiments measures infrared emission in the 3.0-5.0 μm wavelength range. The measured radiation field is converted to temperature field through the emissivity of the surface being measured. The camera is placed around 5 cm from the field of view, in which, the hot moving nozzle dispenses the new PLA layer. The temperature field is measured at a rate of 30 frames per second. Since the accuracy of infrared-based temperature measurement depends critically on the quality of calibration, an extensive calibration is carried out in advance of the experiments. The infrared camera is used to measure the temperature of a PLA sample maintained at a number of well-known temperatures using an Instec HCS622V thermal stage. The emissivity of PLA is determined as the value that results in best agreement between the known set temperatures and measured temperatures by the infrared camera in these calibration measurements.

The determined emissivity of 0.92 is used throughout the experiments.

Experiments are also carried out to investigate the effect of heating on the mesostructure of the filaments and thermal and mechanical properties of the printed sample. For measurement of thermal properties, samples of size 40 mm by 40 mm and 10 mm are printed with combined preheater and postheater configuration at 1.95 mm gap, as well as the no-heater, baseline case. In order to reveal the filament cross-section in each case, the printed samples are cut using liquid Nitrogen as described in a recent paper [21]. Briefly, the samples are dipped in liquid Nitrogen for 10 minutes, followed by impact load on a notch, which results in a clean cut of the sample without blurring of the cross-section that would have occurred in case of a heat-generating cutting process such as sawing. Thermal resistance of printed samples is measured using a one-dimensional heat flux method, in which the sample is sandwiched between two plates maintained at different temperatures, and thermal resistance is determined through measurement of heat flux through the sample resulting from the temperature difference.

Dogbone samples for measurement of tensile properties are printed with baseline, no-heater settings and with combined preheater-postheater with 0.95 mm gap between the base and heater surface. Test coupons are built based on a modified version of ASTM D638-2a ‘Standard Test Method for Tensile Properties of Plastics’ [60]. Test coupons are 73.68 mm high, 12 mm wide and 3.2 mm thick. Standard print process settings are used and the print speed is chosen to be 33.3 mm/s. Length, width and thickness of the test coupons are aligned with X, Y and Z axes

with respect to the build plate. Tensile testing is carried out on a Shimadzu AGS-X series universal test frame with a high-precision 5 kN load cell. The cross-head speed is set at 0.02 mm/min. All tests were conducted with stroke-controlled mode. Samples are gripped using a pair of mechanical grips. No grip-failure is observed. Load and displacement data are collected using a standard data acquisition system. Collected data are then post-processed to obtain stress-strain curves.

4.2. Analytical and Numerical Modeling

Temperature rise in previously deposited layers during the deposition of a new filament layer occurs due to two distinct heat sources [52]. The first mechanism is the diffusion of thermal energy contained in the hot dispensed filament. Further, heat transfer also occurs from the hot nozzle through the small air gap into the bed. The latter is a potentially dominant mechanism due to the close promixity between the bed and the rastering nozzle. Similar to heating due to hot nozzle, the presence of the hot preheater or postheater in these experiments is expected to contribute towards temperature rise. As a result, two distinct approaches are taken for modeling the contributions of these mechanisms towards temperature rise on the previous deposited layer. The effect of thermal energy of the dispensed filament is modeled using a well-known analytical equation, whereas heat transfer from the hot nozzle and pre/post-heater is quantified through a finite-volume simulation model.

4.2.1. Analytical modeling for effect of filament dispense

The theoretical treatment discussed in a recent paper [52] is utilized for modeling the effect of hot filament dispense on the temperature distribution. Based on well-known theory of moving heat sources [43,44], temperature distribution due to diffusion of thermal energy in the hot deposited filament can be computed by analyzing the problem in a coordinate system that travels along with the moving nozzle. By solving the governing energy conservation equation subject to appropriate boundary conditions, temperature distribution along the raster line can be shown to be [52]

$$T = T_o + \frac{\dot{q}}{2\pi k \cdot |x - u_x t|} exp\left[-\frac{u_x(|x - u_x t| + x - u_x t)}{2\alpha}\right] \qquad (14)$$

where T_0 is the ambient temperature, u_x is the nozzle speed in the x direction, k and α are thermal conductivity and thermal diffusivity respectively. $\dot{q}$ is the rate at which thermal energy is deposited along with the filament, given by [52]

$$\dot{q} = \int_{T_0}^{T_n} \dot{m} C_p \, dT \qquad (15)$$

where $\dot{m}$ is the mass flow rate, C_p is the filament heat capacity and T_n is the nozzle temperature.

4.2.2. Finite-volume modeling

Due to the geometrical complexity of the nozzle and pre/postheater assembly, it is difficult to derive an analytical equation for heat transfer into and subsequent temperature rise of the previously deposited filament layers. A finite-volume simulation model is developed to account for these effects. These simulations are carried out in ANSYS Fluent, where the motion of the nozzle and pre/post-heater assembly is simulated using dynamic mesh motion. A new mesh is generated at each time step as the nozzle and pre/post-heater moves through the ambient air, resulting in geometrical changes over time. In this case, the motion is described simply by a linear velocity.

A simulation model of the geometry, including the nozzle and pre/post-heater assembly, PLA base and ambient air is created. The nozzle and pre/post-heater are maintained at a fixed temperature of 205 °C, consistent with experimental conditions. The initial temperature of the PLA base is set at 30 °C. Convective heat transfer boundary conditions are applied on the sides of the PLA base, with a convection coefficient of 10 W/m^2K, consistent with natural convection conditions in experiments.

Motion of the nozzle and pre/postheater assembly is implemented using a user-defined function that specifies constant speed rigid body motion in the x direction. Dynamic layering mesh motion method is utilized for temperature computation. It is ensured that boundary displacement between successive

timesteps is much smaller than local cell sizes in order to avoid cell degeneration and negative cell volume. At each timestep, local remeshing is carried out for each cell that is significantly affected by the rigid body motion, for example due to excessive skewing or exceeding the limits of minimum and maximum size criteria. Figure 4.3 presents pictures of the finite volume model, showing the nozzle, preheater, PLA layer underneath and ambient air. As shown, the mesh is designed to be particularly fine around the nozzle and preheater in order to accurately account for heat transfer in the thin layer of air.

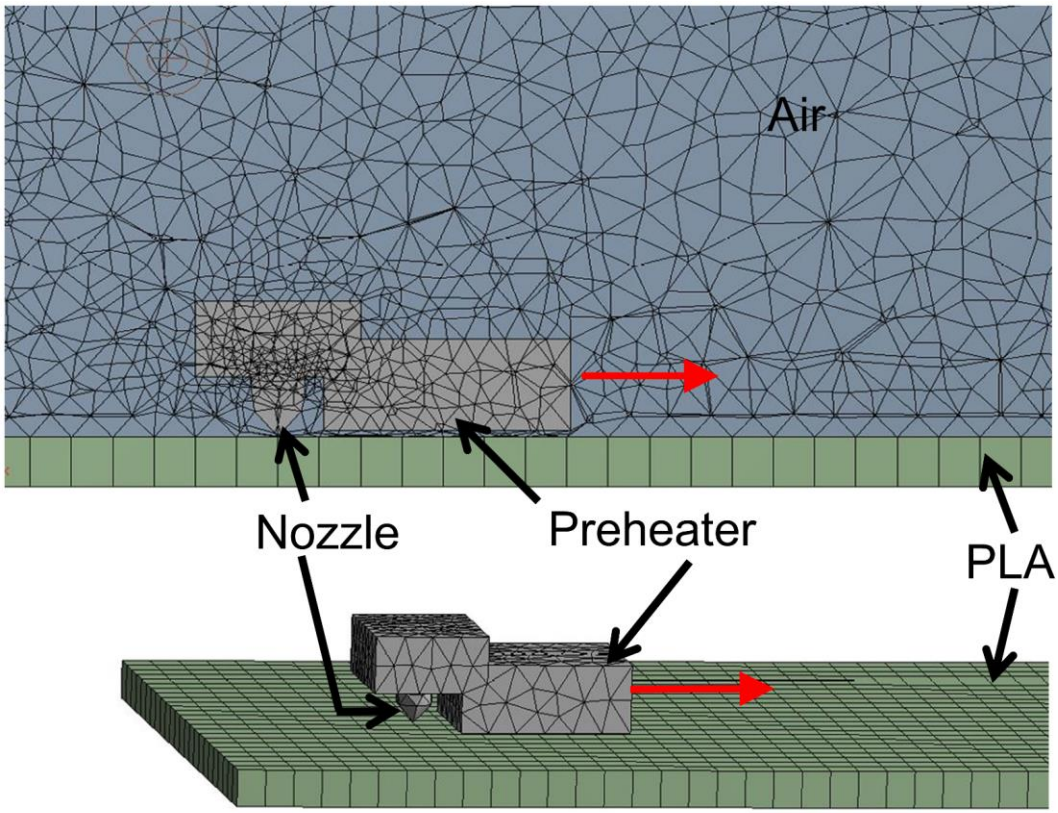

Figure 4.3. Finite-volume simulation setup showing the geometry and meshing.

4.3. Results and discussion

4.3.1. Effect of preheater and postheater configurations on temperature distribution

The effect of preheater and postheater configurations on temperature distribution along the raster line is studied through a number of experiments.

Figure 4.4(a) presents temperature measurement at a fixed location on the print bed surface and along the raster line as a function of time in the preheater configuration, wherein the hot metal block travels ahead of the dispensing nozzle. Temperature is plotted for two different heater-to-base gaps – 0.95 mm and 1.95 mm – at a fixed raster speed of 4.1 mm/s. For comparison, temperature measurement corresponding to the baseline case without preheating at the same raster speed is also plotted. In each of the three cases plotted in Figure 4.4(a), temperature rises slowly as the nozzle approaches the point of interest, followed by a sharp rise and peak corresponding to the time at which the filament is dispensed at the point of interest. Subsequently, there is a gradual decline in temperature as the nozzle moves away from the point of interest. These characteristics are all consistent with measurements reported in the past, as well as with theoretical predictions from moving heat source theory [52].

The impact of the preheater configuration is seen clearly in the two plots corresponding to preheater configurations in Figure 4.4(a). Both show significant increase in temperature even prior to arrival of the nozzle. The two plateaus in Figure 4.4(a) correspond to additional preheating caused by the preheater

configuration that arrives at the point of interest prior to the nozzle. After the nozzle has passed the point of interest, temperature reduces for all three cases following the same general trend. There is some additional temperature increase in the two curves corresponding to the preheater configurations compared to the baseline, which is likely due to diffusion of thermal energy absorbed from the preheater even before nozzle arrival.

Further, Figure 4.4(a) shows that the temperature increase due to preheater configuration is a function of the heater-to-base gap. In the two cases studied here, the lower gap results in higher temperature rise, which is along expected lines because of increased conduction and radiation heat transfer between the hot preheater surface and the raster plane. Conduction heat transfer increases due to increased temperature gradient, whereas radiative heat transfer increases due to increased radiative view factor between the two surfaces at lower gap. Figure 4.4(a) provides evidence of enhanced temperature rise due to the preheater configuration, which may be expected to result in increased filament-to-filament bonding.

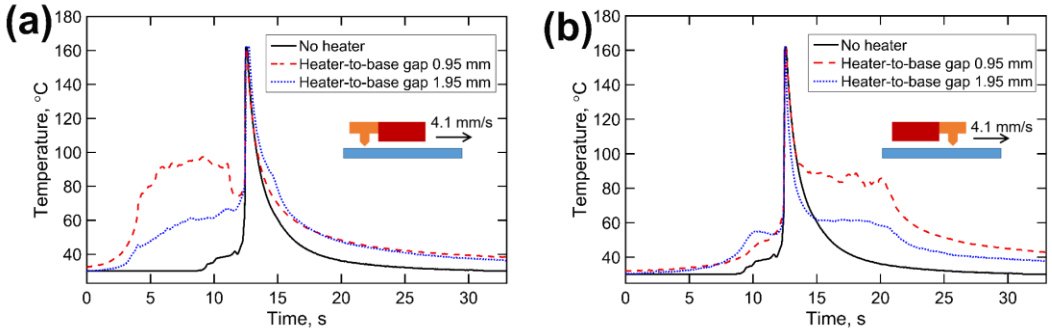

Figure 4.4. Measured temperature as a function of time at a fixed point on the raster line for two different heater-to-base gaps. For reference, the baseline case without additional heating is also shown. (a) and (b) show data for preheater and postheater configurations, respectively.

Similar experiments are then carried out to understand the thermal impact of postheater configuration. A fixed raster speed of 4.1 mm/s and heater-to-base gaps of 0.95 mm and 1.95 mm are utilized, similar to Figure 4.4(a). Postheater configuration data are plotted in Figure 4.4(b), along with a baseline case with no additional heating. The impact of the postheater configuration on temperature distribution after filament dispense is clearly seen in Figure 4.4(b). There is greater temperature rise for the lower gap case, as expected, due to greater rate of conduction and radiative heat transfer enabled by the small gap. The postheater configuration does not significantly impact temperature before filament dispense, because minimal heat transfer is expected at the point of interest until the nozzle has passed and the postheater appears above the point. This is similar to the preheater configuration case, where there was relatively lower impact of temperature after filament dispense.

To further understand the thermal impact of preheater and postheater configurations, experiments are carried out for the two configurations at multiple raster speeds. Figure 4.5(a) plots temperature as a function of time at a fixed point on the raster line for the preheater configuration at three different raster speeds. The heater-to-base gap is fixed at 0.95 mm. Measurement for the baseline case without preheating is also plotted for comparison. Similar to Figure 4.4(a), at each raster speed, a significant temperature plateau is observed prior to the peak, while the peak temperature does not change much. The area under the temperature-time

curve, which roughly corresponds the total thermal dose, or energy, transferred into the previous deposited layers is significantly increased by the use of the preheater, particularly at low raster speeds. This is because at low raster speed, the point of interest is exposed to the hot preheater surface for a longer time, which results in a greater width of the plateau region in Figure 4.5(a) prior to the temperature peak. This indicates that a lower raster speed may result in greater duration of elevated temperature prior to filament dispense. The width of this region in all three cases is found to be close to the expected value based on the raster speed in each case and the width of the preheater configuration. Following the temperature peak at the time of filament dispense, temperature reduces gradually, with greater deviation between the two at lower raster speeds. This is likely due to greater thermal energy absorbed in the greater time of exposure at lower raster speeds.

Figure 4.5(b) plots experimental data from similar experiments in the postheater configuration at three different raster speeds. As expected, in these cases, increased temperature rise is observed after the nozzle has passed over the point of interest, because in this case, the postheater trails behind the nozzle and heats up the point of interest after filament dispense. Similar to Figure 4.4(b), relatively lesser impact is observed before filament dispense, and elevated plateau in the temperature plot after filament dispense is found to be the highest for the lowest raster speed investigated in these experiments.

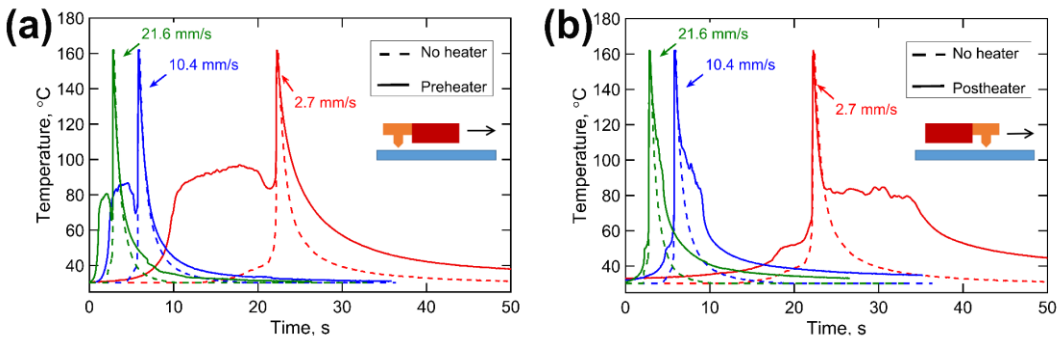

Figure 4.5. Measured temperature as a function of time at a fixed point on the raster line for three raster speeds. For reference, the baseline case without additional heating is also shown. (a) and (b) show data for preheater and postheater configurations, respectively. Broken and solid lines correspond to the baseline and heater cases respectively, while colors correspond to three different raster speeds.

Finally, these experiments are carried out for a combined preheater-postheater configuration. A comparison of the combined configuration with preheater-only and postheater-only is presented in Figures 4.6(a) and 4.6(b) for two different raster speeds. These plots show that the presence of both configurations results in significant increase in temperature at the point of interest both before and after filament dispense. The preheater-postheater configuration offers the benefits of both individual configurations. As expected, time duration for which increased temperature is observed is lower for higher raster speed (Figure 4.6(a) vs. Figure 4.6(b)), which is explained by the shorter exposure time at higher raster speed. The provisioning of both preheating and postheating configurations incurs only incremental cost and complexity compared to only one. The heating current is expected to go up nominally due to the increased thermal mass to be maintained at a high temperature, but otherwise, this represents a very passive approach for obtaining significant benefits in filament-to-filament bonding.

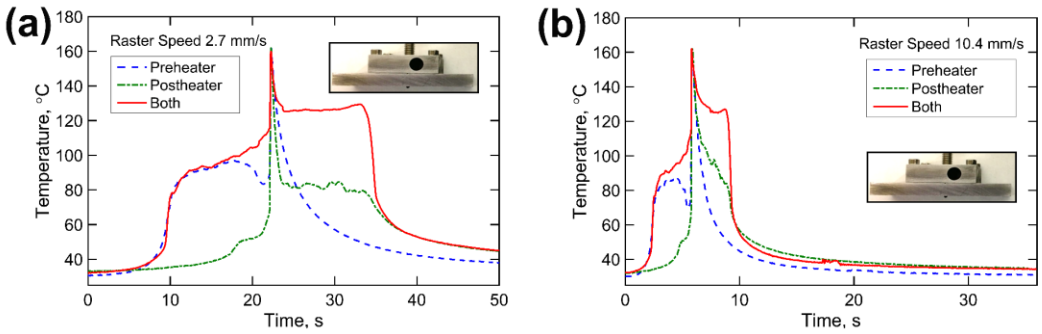

Figure 4.6. Temperature plots comparing the impact of preheater and postheater configurations with a case where both preheater and postheater are used. (a) and (b) show these plots for raster speeds of 2.7 mm/s and 10.4 mm/s respectively.

4.3.1. Analytical/numerical model results and comparison with experimental measurements

Experimental measurements are compared with analytical and numerical models discussed in section 3 that predict temperature distribution at the interface of previous and newly deposited layer. These models account for temperature rise due to two independent effects separately – thermal energy in the deposited filament and heat transfer from the hot nozzle and pre/post heaters. While a previously reported analytical model [52] is used for computing the effect of thermal energy in the deposited filament, a finite-volume simulation model is used for the effect of the hot nozzle and pre/post heaters due to the considerable geometrical complexity. Figure 4.7 presents colorplots of the temperature distribution predicted by the finite-volume simulation model at three different times while the nozzle-preheater assembly rasters along a straight line from left to right. While one set shows a cross-section view, the other set shows the temperature profile on the base surface in an isometric view while showing only an outline of the preheater and nozzle assembly.

These plots clearly show the thermal influence of the preheater. Temperature on the base surface directly underneath the preheater block is significantly elevated. While the thermal impact of the preheater block does not extend much beyond its footprint, the effect is highly directed and heats up precisely the region at which the filament is about to be dispensed. Further, the size of the preheater block can potentially be changed in order to change the size of the zone of thermal influence. As the preheater-nozzle assembly moves from left to right, the heated zone on the base surface also moves. The preheater effectively preheats the base surface before filament is dispensed, which may be very effective for promoting filament-to-filament adhesion.

Figures 4.8 present comparison between experimental measurements and analytical/numerical model. Thermal conductivity, specific heat and density of the PLA platform are taken to be 0.2 W/mK, 1800 J/kgK and 1300 kg/m^3. The nozzle and preheater block are assumed to be maintained at 205 ^{o}C. Heat transfer due to convective motion in the ambient air is neglected. Figure 4.8 plots experimentally measured and theoretically predicted temperature distribution along the raster line at two different times for fixed heater-to-base gap of 0.95 mm and raster speed of 10.4 mm/s. In both cases, there is good agreement between measurements and modeling. As shown, the theoretical model predicts infinite temperature at the location of the filament due to the presence of a singularity at $x = u_x \cdot t$ in equation (1), which is the reason behind the deviation close to the location of the filament. Several possible sources of error exist in both experiments and modeling. For

example, the finite-volume model does not account for microscale surface finish of the heater that may play an important role in heat transfer across the small gap. The simulation model does not account for radiative heat transfer across the air gap. Further, the model assumes the filament deposition process to deposit a point source of heat, whereas in experiments, the heat source is likely to be somewhat more distributed. Finally, measurement errors associated with infrared thermometry may also exist. Within the limitations of these sources of error, Figure 4.8 represents good agreement between measurements and modeling.

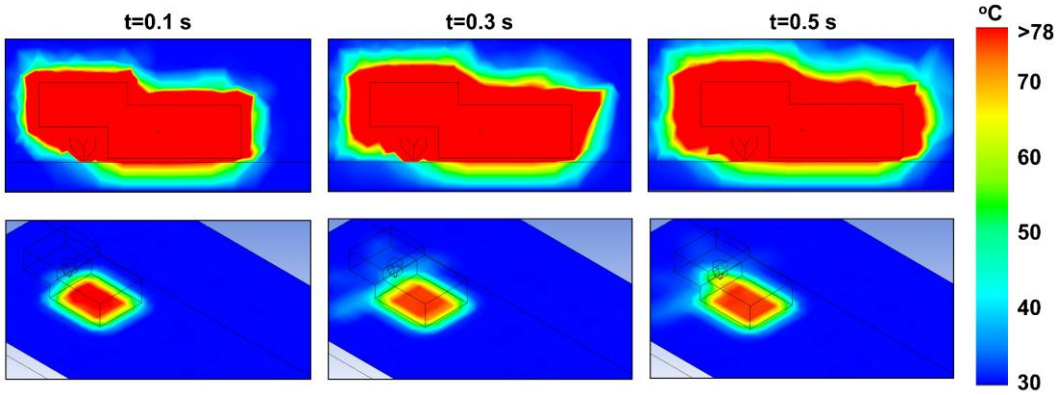

Figure 4.7. Colorplots showing temperature distribution predicted by the finite-element simulation at three different times while the nozzle-preheater assembly rasters along a straight line.

4.3.2. Effect of pre/post heating on filament interlayer bonding

The key motivation behind the design of the preheater and postheater configurations is to supply additional thermal energy to the raster lines, and therefore increase the effectiveness of merging between adjacent filaments. While Figures 4.4-4.8 clearly present evidence of increased temperature along the raster line due to the preheat and postheater configurations, further experiments are also

carried out to investigate the effect of this temperature rise on the filament mesostructure and eventually on functional properties of the printed parts.

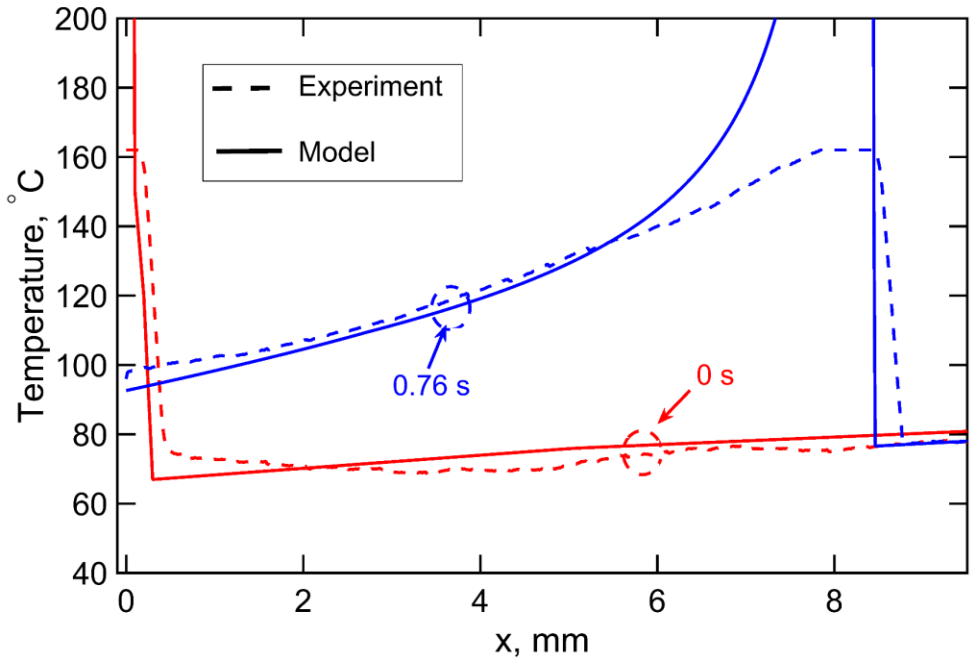

Figure 4.8. Comparison of experimental temperature measurement along the raster line on the bed surface with predictions based on the analytical and finite-element simulation models. Temperature profile is plotted at two different times for the case for dispensing with preheater.

Figure 4.9 presents cross-section images for the baseline case and for a combined preheater-postheater configuration at 60 mm/s raster speed and 0.95 mm gap from the heater surface and base. These images clearly show evidence of increased filament-to-filament necking (i.e. increase in negative gap between adjacent filaments) due to the thermal effect of the preheater and postheater configurations. In order to estimate the fraction of voiding in the baseline and combined preheater-postheater samples, representative void spaces in Fig. 9 are filled with variable size diamonds of known area. The sum of the diamond-occupied

area represents the approximate area of voids. Table 1 outlines the calculated area fraction of the voided area in the two samples. These data show that significant reduction in the fraction of void area from 0.23 in the baseline samples to 0.067 in the combined preheater-postheater sample.

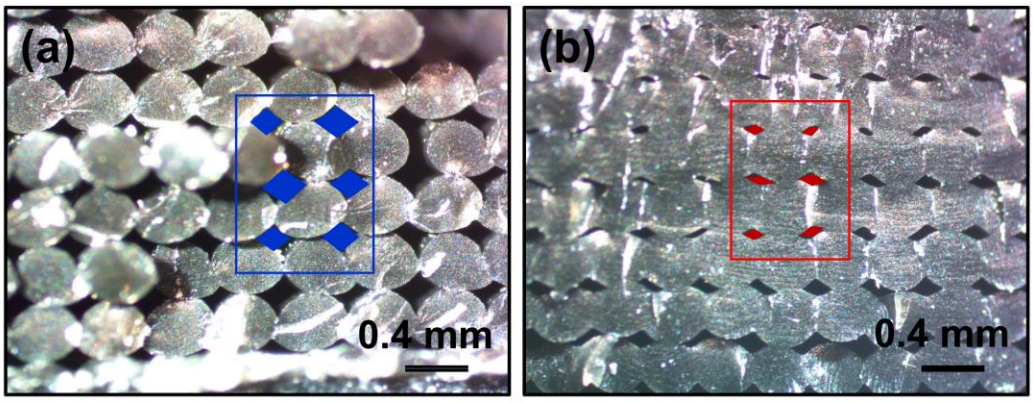

Figure 4.9. Cross-section images showing the impact of pre/post heating on filament-to-filament bonding. (a) shows the baseline case, while (b) shows the case with pre/post heating. In this case, the raster speed is 60 mm/s and heater-to-base gap is 0.95 mm.

Table 4.1: Estimated area fraction of the voided area in the baseline no-heater and combined preheater-postheater samples

Sample Type	Area of Representative Volume Element (cm^2), A_R	Area of Void (cm^2), A_V	Void Area Fraction, v_{void}
No Heater	9.9	2.28	0.230
Combined Preheater-postheater	6.5	0.44	0.067

Further, Figure 4.10 plots measured thermal resistance of printed samples as a function of sample thickness for both baseline samples without heater, as well

as samples printed with a combined preheater-postheater. Data clearly show significant reduction in values of thermal resistance as well as the slope as a result of the combined preheater-postheater. Based on the reduced slope, the combined preheater-postheater results in around 22% increase in thermal conductivity. The improvement correlates well with the improved filament-to-filament bonding shown in Figure 4.9, since it is well-known that interfacial thermal transport between filaments plays a key role in determining overall thermal performance of the part [27]. The significant improvement in thermal performance demonstrated here may be critical for applications where the part is expected to withstand thermal loads.

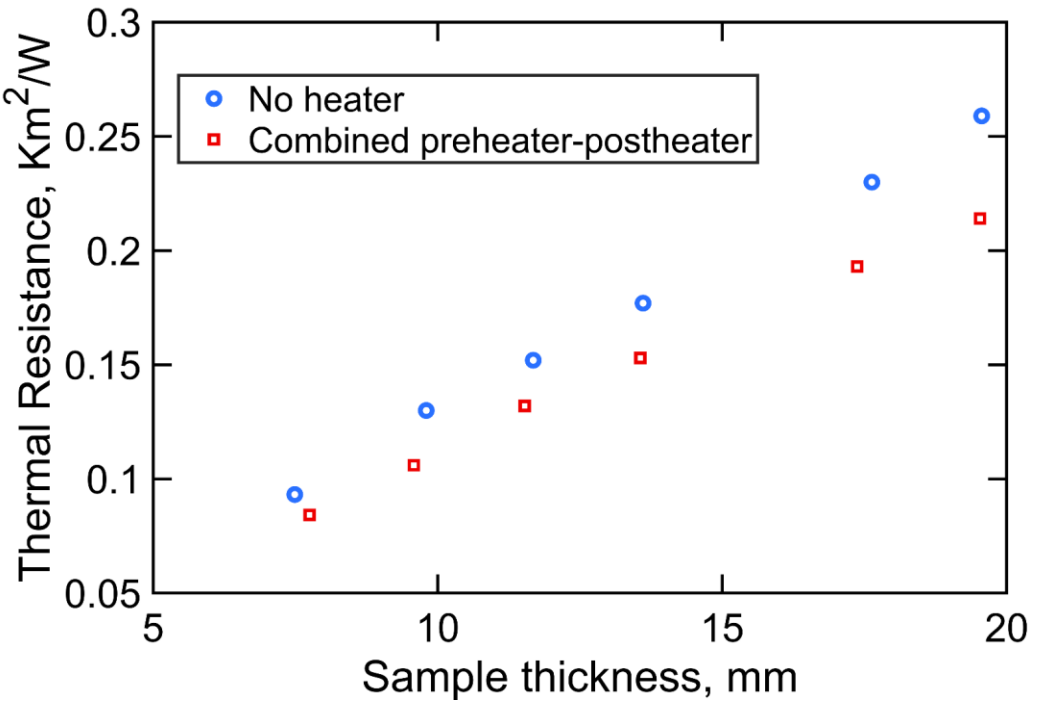

Figure 4.10. Variation of measured thermal resistance of printed samples with sample thickness. Data are presented for both baseline samples as well as those printed with combined pre-heater and post-heater. Reciprocal of the slope of the curves is indicative of thermal conductivity of the samples.

Finally, Figure 4.11 plots stress-strain curves for a baseline sample and a combined preheater-postheater sample, both printed at 33.3 mm/s speed. These measurements were carried out by Viswajit Talluru and Dr. Ashfaq Adnan. The resulting mechanical properties are also summarized in Table 2, showing 60% and 165% improvement in Ultimate Tensile Stress and Modulus of Toughness, respectively. Such improvement arises directly from improved filament-to-filament bonding and reduced void area fraction as shown in Figure 4.9. This is consistent with recent work [61] that shows 85% reduction in stress intensity of singularity points between adjacent filaments due to an increase in filament-to-filament gap setting from 0.1% to 1%. The 164% increase in modulus of toughness also supports the premise of improved filament-to-filament bonding due to preheater and postheating by the in situ heater.

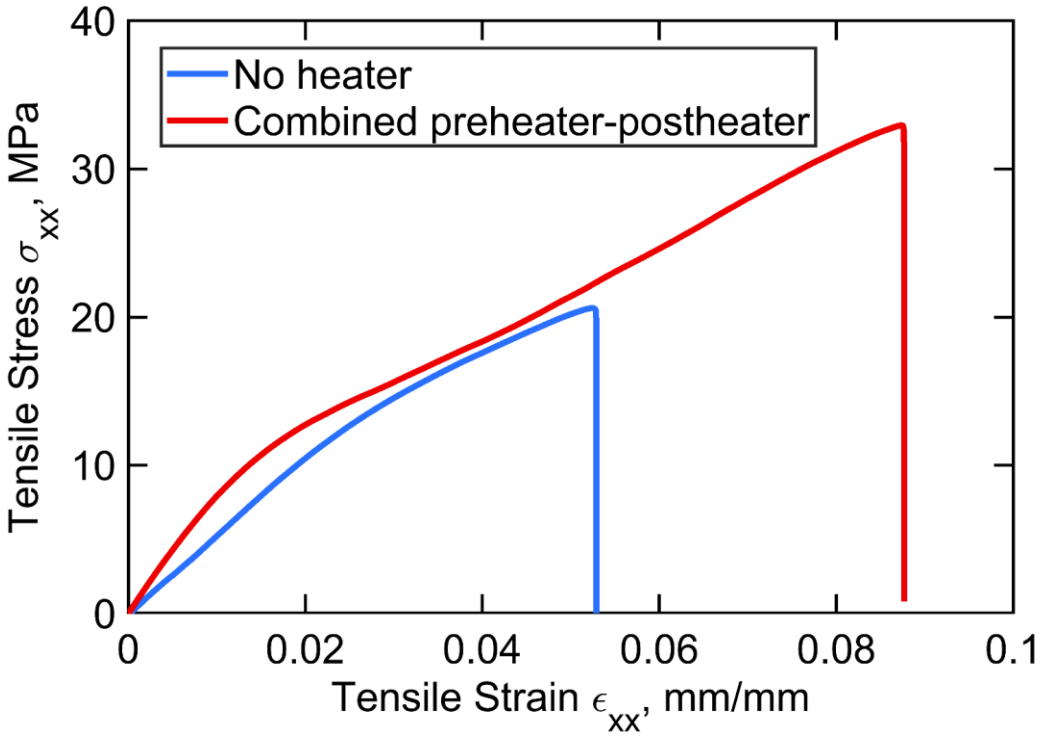

Figure 4.11. Stress-vs-strain plot for samples printed at 3600 mm/min scan speed for both baseline case and with preheater-postheater configuration, showing significant improvement in strength and toughness.

Table 4.2: Measured mechanical properties of the baseline no-heater and combined preheater-postheater samples. The percentage improvement for each property is listed within brackets.

Sample Type	Young's modulus, E (MPa)	Ultimate tensile strength (MPa)	Modulus of Toughness (kPa)
No Heater	512	20.6	625
Combined preheater-postheater	844 (65%)	32.9 (60%)	1655 (165%)

While experiments carried out in this work make a distinction between preheater and postheater configurations because only a single filament line is being rastered, it must be recognized that such a distinction may not exist in practical scenarios where multiple lines are being sequentially rastered. This is because typically the nozzle travels in a U configuration, so that when one line is rastered from left to right, the next is rastered from right to left. This results in the preheater configuration in the first line effectively acting as a postheater configuration in the next line when the travel direction of the nozzle reverses. Therefore, it is expected that even a single metal heater may result in combined preheater/postheater effects. Due to the simplicity of the design of the heating mechanism studied here compared to past efforts for external heating [57,58,59], it is certainly possible to include both preheater and postheater configurations, such as shown in the inset of Figure 4.6, in order to maximize the thermal benefit without much incremental cost or effort.

CONCLUSIONS

Chapter 2 combines *in situ* high speed imaging of the polymer extrusion based additive manufacturing process with post-print thermal conductivity measurements to investigate the relationships between process parameters, microstructure and eventual properties of the built part. Given the significant design flexibility enabled by additive manufacturing, a thorough understanding of these relationships is critical in order to maximize the benefit of additive manufacturing within the feasible design space. This becomes even more important in the case of multifunctional parts where more than one properties of the built part must be balanced with other considerations such as processing time, weight, etc., all within the given feasible parametric space of manufacturability. The present work enables such optimization by developing relationships between process parameters and thermal properties of interest in a variety of applications. Results indicate strong dependence of build direction thermal conductivity on various process parameters such as raster speed, layer height, etc. In addition to improving the fundamental understanding of polymer extrusion based additive manufacturing process, this work may also enable the printing of parts with novel thermal transport properties.

Chapter 3 investigates heat transfer on the platform bed during filament deposition in polymer extrusion additive manufacturing. Quantification of the contributions of two distinct heat transfer mechanisms to temperature rise offers key insights into the nature of heat transfer in this process. Good agreement between experimental data and theoretical model over a broad range of parameters

is demonstrated. Experimental methods and data from this work may be used for optimizing and improving polymer AM processes by ensuring good filament-to-filament bonding, and hence, good ultimate properties of the built part. For example, based on results from this work, process parameters could be manipulated in order to obtain desired filament-to-filament bonding. When optimized carefully, this may lead to parts with novel, spatially varying orthotropic properties. Further, a good understanding of heat transfer during polymer AM processes can also be used for printing parts with novel, multifunctional properties, which is particularly helpful in applications that call for multi-functional components.

Chapter 4 investigates a novel technique for providing additional heating to previously deposited layers in polymer additive manufacturing. This technique utilizes a hot metal block rastering ahead of and/or behind that is much simpler compared to other approaches such as laser heating or microwave heating that have been presented in the past. Infrared thermography clearly shows the significant impact of this approach on the temperature distribution in the previously deposited layer. A combined approach that integrates both preheater and postheater configurations may be of particular interest as it combines the thermal benefits of both configurations with minimal additional cost or complexity. Experimental data are shown to be in good agreement with modeling results. The increased thermal energy into the part is shown to have a clear impact on the filament mesostructure.

This approach can potentially be used for improving thermal and mechanical properties of parts built using polymer AM processes. Through careful

process optimization, this may result in parts with novel thermal and mechanical properties that are not possible through conventional polymer AM processes.

REFERENCES

[1] J.P. Kruth, M.C. Leu, T. Nakagawa, ‘Progress in Additive Manufacturing and Rapid Prototyping,’ *CIRP Annals Manufac. Technol.,* 2, 1998, pp. 525-540.

[2] K.V. Wong, A Hernandez, ‘A Review of Additive Manufacturing,’ *ISRN Mechanical Engineering,* 1, 2012, pp. 1-10.

[3] W.E. Frazier, ‘Metal Additive Manufacturing: A Review,’ *J. Mater. Eng. & Performance,* 23, 2014, pp. 1917–1928.

[4] N. Guo, M.C. Leu, ‘Additive manufacturing: technology, applications and research needs,’ *Frontiers of Mechanical Engineering,* 8, 2013, pp. 215–243.

[5] H.J. Timothy, H.L.A Ola, ‘Overview of current additive manufacturing technologies and selected applications,’ *Science Progress,* 95, 2012, pp. 255-282.

[6] O. Ivanova, C. Williams, T. Campbell, ‘Additive manufacturing (AM) and nanotechnology: promises and challenges,’ *Rapid Prototyping J.,* 19, 2013, pp. 353-364.

[7] V. Petrovic, J.V.H. Gonzalez, O.J. Ferrando, J.D. Gordillo, J.R.B. Puchades, L.P. Griñan, ‘Additive layered manufacturing: sectors of industrial application shown through case studies,’ *Int. J. Production Res.,* 49, 2011, pp. 061–1079.

[8] N.K. Tolochko, M.K. Arshinov, A.V. Gusarov, V.I. Titov, T. Laoui, L. Froyen, ‘Mechanisms of selective laser sintering and heat transfer in Ti powder,’ *Rapid Prototyping J.,* 9, 2003, pp. 314-326.

[9] J.P. Kruth, X. Wang, T. Laoui, L. Froyen, ‘Lasers and materials in selective laser sintering,’ *Assembly Automation,* 23, 2003, pp. 357-371.

[10] F. Ning , W. Cong, J. Qiu, J. Wei, S. Wang, ‘Additive manufacturing of carbon fiber reinforced thermoplastic composites using fused deposition modeling,’ *Composites Part B,* 80, 2015, pp. 369-378.

[11] S. Upcraft, R. Fletcher, 'The rapid prototyping technologies,' *Assembly Automation,* 23, 2003, pp. 318-330.

[12] K. Thrimurthulu, P.M. Pandey, N.V. Reddy, 'Optimum part deposition orientation in fused deposition modeling,' *Int. J. Machine Tools & Manufac.,* 44, 2004, pp. 585–594.

[13] J.W. Stansbury, M.J. Idacavagec, '3D printing with polymers: Challenges among expanding options and opportunities,' *Dental Mater.,* 32, 2016, pp. 54-64.

[14] B.H. Lee, J. Abdullah, Z.A. Khan, 'Optimization of rapid prototyping parameters for production of flexible ABS object,' *J. Mater. Processing Technol.,* 169, 2005, pp. 54-61.

[15] C. Bellehumeur, L. Li, Q. Sun, P. Gu, 'Modeling of Bond Formation Between Polymer Filaments in the Fused Deposition Modeling Process,' *J. Manufac. Processes,* 6, 2004, pp. 170-178.

[16] Q. Sun, G.M. Rizvi, C.T. Bellehumeur, P. Gu, 'Effect of processing conditions on the bonding quality of FDM polymer filaments,' *J. Manufac. Processes,* 14, 2008, pp. 72-80.

[17] M. Nikzada, S.H. Masooda, I. Sbarskia, A. Grothb, 'A Study of Melt Flow Analysis of an ABS-Iron Composite in Fused Deposition Modelling Process,' *Tsinghua Science & Technol.,* 14, 2009, pp. 29-37.

[18] H. Bikas1, P. Stavropoulos, G. Chryssolouris, 'Additive manufacturing methods and modelling approaches: a critical review,' *Int. J. Advanced Manufac. Technol.,* 83, 2016, pp. 389–405.

[19] S. Ahn, M. Montero, D. Odell, S. Roundy, P.K. Wright, 'Anisotropic material properties of fused deposition modeling ABS,' *Rapid Prototyping J.,* 8, 2002, pp. 248-257.

[20] R. Anitha, S. Arunachalam, P. Radhakrishnan, 'Critical parameters influencing the quality of prototypes in fused deposition modelling,' *J. Mater. Processing Technol.*, 118, 2001, pp. 385-388.

[21] A.K. Sooda, R.K. Ohdar, S.S. Mahapatrac, 'Parametric appraisal of mechanical property of fused deposition modelling processed parts,' *Materials & Design*, 31, 2010, pp. 287-295.

[22] F. Ning, W. Cong, Y. Hu and H. Wang, 'Additive manufacturing of carbon fiber-reinforced plastic composites using fused deposition modeling: Effects of process parameters on tensile properties,' *J. Composite Mater.*, 51, 2016, pp. 451-462.

[23] A.K. Sooda, R.K. Ohdar, S.S. Mahapatra, 'Experimental investigation and empirical modelling of FDM process for compressive strength improvement,' *J. Adv. Res.*, 3, 2012, pp. 81-90.

[24] B.M. Tymrak, M. Kreiger, J.M. Pearce, 'Mechanical properties of components fabricated with open-source 3-D printers under realistic environmental conditions,' *Materials & Design*, 58, 2014, pp. 242-246.

[25] F.P. Incropera, D.P. DeWitt, T.L. Bergman, A.S. Levine, Introduction to Heat Transfer, John Wiley & Sons, 5th Ed., 2006.

[26] V. Vishwakarma, C. Waghela, A. Jain, 'Measurement of out-of-plane thermal conductivity of substrates for flexible electronics and displays,' *Microelectronic Eng*, 142, 2015, pp. 36-39, 2015. (DOI: 10.1016/j.mee.2015.06.008).

[27] H. Prajapati, D. Ravoori, R. Woods, A. Jain, 'Measurement of Anisotropic Thermal Conductivity and Inter-Layer Thermal Contact Resistance in Polymer Fused Deposition Modeling (FDM),' *Additive Manufac.*, in press, 2018.

[28] D.T. Pham, R.S. Gault, 'A comparison of rapid prototyping technologies,' *Int. J. Machine Tools & Manufacture*, 38, 1998, pp.1257–1287

[29] N. Guo, M.C. Leu, ‘Additive manufacturing: technology, applications and research needs,’ *Frontiers of Mechanical Engineering*, 8, 2013, pp. 215–243.

[30] I. Zein, D.W. Hutmacher, K.C. Tan, S.H. Teoh, ‘Fused deposition modeling of novel scaffold architectures for tissue engineering applications,’ *Biomaterials,* 4, 2000, pp. 1169-1185.

[31] S. Bose, S. Vahabzadeh, A. Bandyopadhyay, ‘Bone tissue engineering using 3D printing,’ *Materials Today,* 12, 2013, pp. 496-504.

[32] D. Ravoori, L. Alba, H. Prajapati, A. Jain, ‘Investigation of Process-Structure-Property Relationships in Polymer Extrusion Based Additive Manufacturing Through In Situ High Speed Imaging and Thermal Conductivity Measurements,’ *Additive Manufacturing,* 23, 2018, pp. 132-139.

[33] B.G. Compton, B.K. Post, C.E. Duty, L. Love, V. Kunc, ‘Thermal analysis of additive manufacturing of large-scale thermoplastic polymer composites,’ *Additive Manufacturing,* 17, 2017, pp. 77-86.

[34] S.F. Costa, F.M. Duarte, J.A. Covas, ‘Estimation of filament temperature and adhesion development in fused deposition techniques,’ *J. Mater. Processing Technol.*, 245, 2017, pp. 167-179.

[35] D. Anthony, D. Wong , D. Wetz , A. Jain, ‘Non-invasive measurement of internal temperature of a cylindrical Li-ion cell during high-rate discharge,’ *International Journal of Heat and Mass Transfer*, 111, 2017, pp. 223-231.

[36] L. Dupont, Y. Avenas, P. Jeannin, ‘Comparison of Junction Temperature Evaluations in a Power IGBT Module Using an IR Camera and Three Thermosensitive Electrical Parameters,’ *International Journal of Heat and Mass Transfer*, 49, 2013, pp. 1599-1608.

[37] H.F. Hamann, A. Weger, J.A. Lacey, Z. Hu, P. Bose, E. Cohen, J. Wakil, ‘Hotspot-limited microprocessors: direct temperature and power distribution measurements,’ *IEEE J. Solid State Circuits*, 42, 2007, pp. 56-65.

[38] J.E. Seppala, K.D. Migler, ‘Infrared thermography of welding zones produced by polymer extrusion additive manufacturing,’ *Additive Manufacturing*, 12, 2016, pp. 71-76.

[39] H. Prajapati, D. Ravoori, A. Jain, ‘Measurement and modeling of filament temperature distribution in the standoff gap between nozzle and bed in polymer-based additive manufacturing,’ *Additive Manufacturing*, 24, pp. 224-231, 2018.

[40] J. Go, S.N. Schiffres, A.G. Stevens, A.J. Hart, ‘Rate limits of additive manufacturing by fused filament fabrication and guidelines for high-throughput system design,’ *Additive Manufacturing*, 16, 2017, pp. 1-11.

[41] M.E. Mackay, Z.R. Swain, C.R. Banbury, ‘The performance of the hot end in a plasticating 3D printer,’ *J. Rheology*, 61, 2017, pp. 229-236.

[42] A. D’Amico, A.M. Peterson, ‘An adaptable FEA simulation of material extrusion additive manufacturing heat transfer in 3D,’ *Additive Manufaturing*, 21, 2018, pp. 422-430.

[43] N. Özışık, ‘Heat Conduction’, *John Wiley & Sons*, 3rd Ed., 2012.

[44] E. Kannatey-Asibu Jr., ‘Principles of Laser Materials Processing’, *John Wiley & Sons*, 1st Ed., 2009.

[45] J. Mazumder, W. M. Steen, ‘Heat transfer model for cw laser material processing,’ *Journal of Applied Physics*, 51, 1980, pp. 941-947.

[46] X. He, P. W. Fuerschbach, T. Debroy, ‘Heat transfer and fluid flow during laser spot welding of 304 stainless steel,’ *J. Phys. D: Appl. Phys.*, 36, 2003, pp. 1388–1398.

[47] D. Dimitrov, K. Schreve, N. de Beer, ‘Advances in three dimensional printing – state of the art and future perspectives,’ *Rapid Prototyping J.*, 12, 2006, pp. 136–147.

[48] S. Thompson, Z. Aspin, N. Shamsaei, A. Elwany, L. Bian, ‘Additive manufacturing of heat exchangers: A case study on a multi-layered Ti–6Al–4V oscillating heat pipe,’ *Additive Manufacturing*, 8, 2015, pp. 163-174.

[49] C. Duty, C. Ajinjeru, V. Kishore, B. Compton, N. Hmeidat, X. Chen, P. Liu, A. Hassen, J. Lindahl, V. Kunc, ‘What makes a material printable? A viscoelastic model for extrusion-based 3D printing of polymers,’ *Journal of Manufacturing Process*, 35, 2018, pp. 526-537.

[50] A. Costa, A. da Silva, O. Carneiro, ‘A study on extruded filament bonding in fused filament fabrication,’ Rapid Prototyping Journal, 2018. (DOI: 10.1108/RPJ-03-2018-0062).

[51] J. Yin, C. Lu, J. Fu, Y. Huang, Y. Zheng, ‘Interfacial bonding during multi-material fused deposition modeling (FDM) process due to inter-molecular diffusion,’ *Journal of Materials and Design*, 150, 2018, pp.104-112.

[52] D. Ravoori, C. Lowery, H. Prajapati, A. Jain, ‘Experimental and theoretical investigation of heat transfer in platform bed during polymer extrusion based additive manufacturing,’ *Polymer Testing*, 73, 2019, pp. 439-446.

[53] J.E. Seppala, K.D. Migler, ‘Infrared thermography of welding zones produced by polymer extrusion additive manufacturing,’ *Additive Manufacturing*, 12, 2016, pp. 71-76.

[54] H. Prajapati, D. Chalise, D. Ravoori, A. Jain, ’Improvement in build-direction thermal conductivity in extrusion-based polymer additive manufacturing through thermal annealing,’ in review, *Additive Manufacturing*, 2019.

[55] K.R. Hart, R.M. Dunn, J.M. Sietins, C.M.H. Mock, M.E. Mackay, E.D. Wetzel, ‘Increased fracture toughness of additively manufactured amorphous thermoplastics via thermal annealing,’ *Polymer*, 144, pp.192-204, 2018.

[56] M.D. Wolkowicz, S.K. Gaggar, 'Effect of thermal aging on impact strength acrylonitrile-butadiene-styrene (ABS) terpolymer,' *Polymer Engineering & Science*, 21, pp.571-575, 1981.

[57] A. Ravi, A. Deshpande, K. Hsu, 'An in-process laser localized pre-deposition heating approach to inter-layer bond strengthening in extrusion based polymer additive manufacturing,' *Journal of Manufacturing Process*, 24, 2016, pp.179-185.

[58] V. Kishore, C. Ajinjeru, A. Nycz, B. Post, J. Lindahl, V. Kunc, C. Duty, 'Infrared preheating to improve interlayer strength of big area additive manufacturing (BAAM) components,' *Additive Manufacturing*, 14, 2017, pp.7-12.

[59] C. Sweeney, B. Lackey, M. Pospisil, T. Achee, V. Hicks, A. Moran, B. Teipel, M. Saed, M. Green, 'Welding of 3D-printed carbon nanotube–polymer composites by locally induced microwave heating,' *Science Advances*, 6, 2017, pp. 1-6.

[60] https://www.astm.org/Standards/D638.htm, last accessed May 28, 2019.

[61] A. Rezaee, A. Adnan, 'On the elastic stress singularities and mode I notch stress intensity factor for 3D printed polymers,' *Engineering Fracture Mechanics*, 204, 2018, pp. 235-245.

BIOGRAPHICAL INFORMATION

Darshan Ravoori received his B.Tech. degree in Mechanical & Energy Engineering from Vellore Institute of Technology (VIT) India in 2011. Later he worked as Mechanical Engineer from 2011-2015 at QuEST Global across India and USA. He joined University of Texas at Arlington (UT Arlington) as a full-time graduate student in Spring of 2016. His research interests on measurements and enhancement of thermal transport phenomena in polymer based Additive Manufacturing. He also worked as intern at ANSYS INC and Oak Ridge National Lab.

Email: Darshanravoori@gmail.com